

PANCHROMATIC ESTIMATION OF STAR FORMATION RATES IN BZK GALAXIES AT $1 < z < 3$

PETER KURCZYNSKI¹, ERIC GAWISER¹, MINH HUYNH², ROB J. IVISON³, EZEQUIEL TREISTER⁴, IAN SMAIL⁵, GUILLERMO A. BLANC⁶, CAROLIN N. CARDAMONE⁷, THOMAS R. GREVE⁸, EVA SCHINNERER⁸, MEG URRY¹¹, PAUL VAN DER WERF^{9,10}, FABIAN WALTER⁸

Submitted to Astrophysical Journal.

ABSTRACT

We determine Star Formation Rates (SFRs) in a sample of color selected, star forming (sBzK) galaxies ($K_{AB} < 21.8$) in the Extended Chandra Deep Field - South (ECDF-S). To avoid AGN, we eliminate 12% of the original sample that have X-ray detections in Chandra catalogs. Photometric redshift binned, average flux densities are measured with stacking analyses in Spitzer-MIPS IR, APEX/LABOCA sub-millimeter, VLA and GMRT radio and Chandra X-ray (including 4 Ms CDF-S) data. We include averages of aperture fluxes in MUSYC UBVRiz/JHK images to determine UV-through-radio Spectral Energy Distributions (SEDs). We determine total IR luminosities, compare SFR calibrations from FIR, 24 μ m, UV, radio and X-ray wavebands, and we find preferred calibrations for each waveband. We find consistency with our best estimator, SFR_{IR+UV} , to within errors for dust corrected UV and the preferred radio SFR calibration. Our results show that 24 μ m-only and X-ray SFR estimates should be used with caution. Average IR luminosities are consistent with Luminous Infrared Galaxies. We find SFR_{IR+UV} for stacked sBzKs at median redshifts 1.1, 1.4, 1.8, 2.2 to be 12 ± 2.8 , 58 ± 7.0 , 100 ± 14 , 130 ± 28 $M_{\odot} \text{ yr}^{-1}$ respectively. Extrapolated to deeper samples, these galaxies appear to contribute $\sim 20\%$ to the cosmic star formation rate density in the range $1.5 < z \leq 2$.

Subject headings: submillimeter: general, infrared: general, radio continuum: general, galaxies: statistics, galaxies: high redshift

1. INTRODUCTION

The history of star formation traces the origins of visible matter in the universe. Understanding star formation across cosmic time will yield insights into diverse areas of astronomy from the formation and evolution of galaxies to the initial conditions of stellar evolution. The redshift range $1 < z < 3$ is a key epoch in this history, when most of the stars in the universe were born; however, the systematic study of star formation in this range has not yet been accomplished. Galaxies in this range are identified with color selection methods. Estimating their Star Formation Rates (SFRs) is complicated by contamination from Active Galactic Nuclei (AGN), and other sources of systematic uncertainty that include the initial mass

function (IMF; used to extrapolate calibrations based on observations of massive stars to the entire stellar population), photometric redshifts (used to convert flux to luminosity), spectral energy distributions (used to estimate luminosities and correct for dust), and SFR calibrations (used to estimate SFR from the observed luminosity in a particular waveband).

1.1. SFR Calibrations

SFRs are estimated from a wide variety of luminosity calibrations from X-ray through radio wavebands. The most reliable SFR calibration comes from dust extinction corrected, Hydrogen emission line spectroscopy, which measures ionizing UV radiation from young stars (e.g. Calzetti 2008). However, rest frame optical spectroscopy is particularly difficult to obtain for high redshift galaxies. Broadband UV continuum radiation directly probes the light of young stars; however, dust attenuation peaks in the UV and causes both extinction and spectral reddening. Dust attenuated starlight is reprocessed as thermal FIR emission. UV slope based corrections for dust attenuation (e.g. Meurer et al. 1999) are not universally applicable. Low redshift analogs of Lyman Break Galaxies follow this relation (Overzier et al. 2011), although ULIRGs have higher dust correction factors (Howell et al. 2010) and other star forming galaxies have lower dust corrections than expected (e.g. Buat et al. 2010) and significant scatter is observed.

IR luminosity, hereafter defined as $L_{IR} \equiv L(8 - 1000 \mu\text{m})$, estimates dust obscured star formation, but may miss young stars that have escaped their birth clouds. In low SFR galaxies, it may be confused by IR cirrus – emission from old, passive stars that tend to be more uniformly distributed within a galaxy com-

¹ Department of Physics and Astronomy, Rutgers University, Piscataway, NJ 08854, USA

² Infrared Processing and Analysis Center, MS 220-6, California Institute of Technology, Pasadena, CA 91125, USA

³ UK Astronomy Technology Centre, Royal Observatory, Blackford Hill, Edinburgh EH9 3HJ, UK

⁴ Institute for Astronomy, 2680 Woodlawn Drive, University of Hawaii, Honolulu, HI 96822, USA.

⁵ Institute for Computational Cosmology, Department of Physics, Durham University, South Road, Durham DH1 3LE, UK

⁶ Department of Astronomy, The University of Texas at Austin, Austin, USA

⁷ Physics Department, Massachusetts Institute of Technology, Cambridge, MA 02139, USA

⁸ MPI for Astronomy, Königstuhl 17, 69117 Heidelberg, Germany

⁹ Leiden Observatory, Leiden University, PO Box 9513, NL - 2300 RA Leiden, The Netherlands

¹⁰ SUPA, Institute for Astronomy, University of Edinburgh, Royal Observatory, Blackford Hill, Edinburgh EH9 3HJ, UK

¹¹ Department of Physics, Yale University, P.O. Box 208121, New Haven, CT 06520-8121, USA

pared to clumpy star forming regions (Kennicutt 1998a). Because IR and uncorrected UV luminosities sum reprocessed and un-reprocessed photons from star forming regions to yield the total luminosity emitted by young stars, the sum of IR and uncorrected UV SFRs are used to estimate total SFR in high redshift galaxies. This trend follows that used in the local universe where linear combinations of unobscured and obscured SFR estimates are being employed (Kennicutt et al. 2009).

Radio wave (1.4 GHz) luminosity in star forming galaxies, which is unobscured by dust, arises from synchrotron emission from supernova remnants (SNRs; $\sim 90\%$) and thermal free-free emission ($\sim 10\%$), and therefore is linked to young, massive stars (Condon 1992). Some radio wave SFR calibrations (Bell 2003; Yun et al. 2001) and X-ray SFR calibrations (Ranalli et al. 2003) explicitly rely upon empirical correlations between luminosities in their respective wavebands and IR luminosity; therefore, they are indirect measures of IR luminosity.

X-ray emission in star forming galaxies arises from high mass X-ray binaries (HMXBs), consisting of short lived, massive ($M > 8M_{\odot}$) stars with a neutron star companion, low mass X-ray binaries (LMXBs), consisting of long lived, low mass ($M < 1M_{\odot}$) stars with neutron star companions¹² and to a lesser extent, supernova remnants (SNRs) (Persic & Rephaeli 2002). X-ray emission from AGN are major sources of contamination. These multiple sources of X-ray emission, as well as X-ray obscuration by gas and dust, complicate SFR X-ray calibration.

Because of the different assumptions and confounding factors in SFR calibrations, there is a great need for systematic comparison of these methods in high redshift galaxies. In this investigation, we use multiwavelength data to estimate SFRs within a population of high redshift galaxies using a variety of the most commonly used calibrations. By comparing these estimates to the total SFR, estimated from IR and uncorrected UV luminosity, we seek to test their robustness at high redshift.

1.2. sBzK Galaxies

To study star formation in the redshift range of peak star formation density in the universe, we selected BzK galaxies. The BzK color selection criterion (Daddi et al. 2004), has emerged as a successful color based method for identifying galaxies in the range $1.4 \lesssim z \lesssim 2.5$ in a maximally inclusive manner. Daddi et al. (2004) defined the quantity BzK as

$$BzK \equiv (z - K)_{AB} - (B - z)_{AB} \quad (1)$$

They found that actively star forming galaxies, sBzKs, can be selected by requiring $BzK > -0.2$, the upper left region in Figure 1. The reddening vector in the BzK plane is parallel to the BzK line, making this selection unbiased with respect to dust content. The reddest galaxies in both $z-K$ and $B-z$ tend to be old, passively evolving stellar systems at $z > 1.4$ and are known as pBzKs, and are located in the upper right region of Figure 1.

sBzKs have been studied in the Great Observatories Origins Deep Survey (GOODS) (Reddy et al. 2005; Daddi et al. 2007b) (and references therein), Deep3a-F and “Daddi” fields (Dannerbauer et al. 2006; Kong

et al. 2006), United Kingdom Infrared Deep Sky Survey (UKIDSS) (Lane et al. 2007; Dunne et al. 2009), Subaru Deep Field (Hayashi et al. 2007), Subaru/XMM-Newton Deep Field (SXDF) (Takagi et al. 2008), COSMOS (McCracken et al. 2010) and ECDF-S (Blanc et al. 2008; Greve et al. 2010) and the Multiwavelength Survey by Yale-Chile (MUSYC) 1030 and 1255 fields (Blanc et al. 2008).

sBzK galaxies are found in $K_{AB} < 22$ surveys to be typically massive, (stellar mass, $M \sim 10^{11} M_{\odot}$), luminous ($L \sim 10^{11-12} L_{\odot}$) galaxies that are not dominated by AGN. They are highly clustered and moderately abundant, with a surface density of $\sim 1 \text{ arc min}^{-2}$, and a comoving volume density of $\gtrsim 10^{-4} \text{ Mpc}^{-3}$. They are found with a steeply increasing number density with magnitude in the deepest surveys reported.

SFR estimates for this population range from several tens to $600 M_{\odot} \text{ yr}^{-1}$ (see e.g. Daddi et al. 2004, 2005; Reddy et al. 2005), with average SFRs estimated from various methods typically in the range $\sim 100\text{--}200 M_{\odot} \text{ yr}^{-1}$ (Daddi et al. 2005, 2007b; Reddy et al. 2006; Dunne et al. 2009; Pannella et al. 2009; Greve et al. 2010; Yoshikawa et al. 2010). Some individual BzKs have been detected as submillimeter galaxies and estimated at $1000 M_{\odot} \text{ yr}^{-1}$ (Takagi et al. 2008), comparable to the most actively star forming galaxies known.

sBzKs may be important contributors to the cosmic star formation rate density. In order to better understand star formation in these galaxies and their contribution to the cosmic star formation history, we investigate their star formation rates binned according to photometric redshift, and stacked in radio through X-ray wavebands. In particular, we use extensive FIR-submillimeter data, for which we have an improved stacking algorithm (Kurczynski & Gawiser 2010). We discuss observations and data in Section 2. We present our stacking methodology in Section 3, and our methods of estimating luminosities and SFRs in Section 4. Results are presented in Section 5, and we discuss comparisons of SFR, and the contribution of these galaxies to the cosmic star formation rate density in Section 6. Our conclusions are summarized in Section 7. Throughout this paper, magnitudes are measured in the AB system unless stated otherwise. We assume a Salpeter (1955) IMF from $0.1 - 100 M_{\odot}$. Another commonly used IMF, that of Kroupa (2001), would change the slope of the low mass end of the IMF, and multiply the SFRs presented here by factors of 0.58 (e.g. Hopkins 2007). We adopt a cosmology with $\Omega_{\Lambda} = 0.7$, $\Omega_0 = 0.3$, $h_{100} = 0.7$.

2. SAMPLE SELECTION

The Extended Chandra Deep Field - South (ECDF-S) is an extensively studied field in the constellation Fornax (RA $03^{\text{h}}32^{\text{m}}29.0^{\text{s}}$, Dec $-27^{\circ}48'47''$) that was initially observed with the *Chandra X-ray Observatory*. The Multiwavelength Survey by Yale-Chile (MUSYC) provides data for the ECDF-S in UBVRiz/JHK bands (Gawiser et al. 2006). The MUSYC K band source catalog (Taylor et al. 2009) contains more than 8,000 sources with $K_{AB} < 22$ in the ECDF-S with photometric or spectroscopic redshifts. The MUSYC optical catalog (Cardamone et al. 2010) contains $\sim 40,000$ galaxies to $R_{AB} < 25.3$ and includes photometry from 32 bands including 18 medium band optical filters and *Spitzer* Infrared Array

¹² intermediate mass stars $1 < M < 8M_{\odot}$, are not believed to give rise to long lived X-ray luminosity

Camera (IRAC) bands. Photometric redshifts for the optical catalog were obtained with the EAzy software (Brammer et al. 2008) and are estimated to have an average error of $\delta z/(1+z) = 0.009$ based upon comparison with available spectroscopic redshifts from the literature (Cardamone et al. 2010). Photometric or spectroscopic redshifts are assigned to sBzK galaxies by matching positions in the K band source catalog with the MUSYC optical catalog and using redshifts from the optical catalog where redshifts in both catalogs are available.

Our catalog of 725 sBzK galaxies with $K_{Vega} < 20$ ($K_{AB} < 21.8$) is taken from Blanc et al. (2008), and includes 640 (85) galaxies with photometric (spectroscopic) redshifts. Of this sample, 38 galaxies have $z < 0.9$ and are rejected as low redshift contaminants. Individually detected X-ray sources are removed from the sample by cross matching the sBzK positions with the combined Chandra ECDF-S and CDF-S X-ray catalogs; 90 galaxies have an X-ray source within $2''$ radius of the K band position, and thus are rejected as AGN. Possible residual AGN contamination, arising from heavily obscured sources at the highest redshifts, is discussed in Section 5.

Comparison of BzK values from our data set to the original criterion defined by Daddi et al. (2004) requires a color correction. The Bessel B band filter used on the Very Large Telescope (VLT) in the original sample of Daddi et al. (2004) is bluer than the Johnson B band filter on WFI, Suprime-Cam and other instruments, and therefore a color correction must be made to match the BzK criterion in data from these instruments. Not accounting for this correction can lead to an offset of 0.5 mag toward lower values in $(B - z)$ color and 0.04 mag in higher $(z - K)$ color, producing a significant excess of “sBzK” galaxies that are in fact low redshift contaminants (Blanc et al. 2008). The BzK color-color diagram, shown in Figure 1, has colors corrected to be consistent with the Daddi et al. (2004) selection region.

The final sample of 597 sBzKs with redshift $0.9 < z \leq 3.2$ are binned according to redshift into approximately 1 Gyr intervals in cosmic time: $0.9 < z \leq 1.2$, $1.2 < z \leq 1.5$, $1.5 < z \leq 2.0$ and $2.0 < z \leq 3.2$. The redshift binned sets are illustrated in a BzK diagram in Figure 1, and further details are included in Table 1. These sets are used in stacking analyses to determine their aggregate fluxes as discussed below. $(B - z)$ and $(z - K)$ colors for these galaxies are determined from flux values given in the catalog of Blanc et al. (2008). Non-detections in the B band lead to anomalous $(B - z)$ colors for 4 and 13 galaxies in the redshift bins $1.5 < z \leq 2.0$ and $2.0 < z \leq 3.2$, respectively. These galaxies are excluded from Figure 1.

There are 43 sBzK galaxies in the range $z \geq 0.9$ with both photometric and spectroscopic redshifts available. Histograms of photometric and spectroscopic redshift are illustrated in Figure 2. These histograms indicate that the majority of sBzKs fall in the traditional redshift range associated with BzK galaxies, $1.4 < z < 2.5$. There are significant numbers of sBzKs at lower (8%) and higher (26%) redshifts, although BzK selection is less efficient in these ranges. Spectroscopic redshifts are taken from the literature, for which there are substantial selection biases; therefore we do not expect the distribution of spectroscopic redshifts to match precisely the distribution of photometric redshifts. Thus, the trend of spectroscopic

redshifts being distributed at somewhat higher redshifts than the photometric redshifts, apparent from Figure 2, is not necessarily an indication of systematic photometric redshift error.

Photometric redshift errors, defined as $(z_{phot} - z_{spec})/(1 + z_{spec})$, are well described by a Gaussian with mean = -0.02 and $\sigma = 0.08$ among the 43 sBzKs for which both redshifts are available, see Figure 3. Photometric redshift error for these galaxies is plotted vs. spectroscopic redshift in Figure 3, and compared to the distribution of photometric redshift errors for the larger sample of 1285 K selected galaxies with both redshifts available. 1σ and 2σ regions are indicated by shading in the figure. Three sBzK galaxies have photometric redshifts that are more than 2σ outliers.

3. MULTIWAVELENGTH ANALYSES AND STACKING ANALYSES

We measure the multiwavelength spectral energy distributions of our sample of 597 redshift binned sBzK galaxies, and we use these data to trace star formation as a function of redshift. Most of these galaxies are not individually detected in X-ray, far IR-submillimeter and radio wavebands; therefore, stacking analysis, using the K band positional priors, is essential.

UV-Optical-NIR. MUSYC 5σ imaging depths are $U = 26.5$, $B = 26.9$, $V = 26.6$, $R = 26.3$, $I = 24.8$, $z' = 24.0$, $J = 23.1$, $H = 22.4$, $K = 22.4$. Details on the imaging can be found in Gawiser et al. (2006) and Taylor et al. (2009). Galaxies are individually measured in MUSYC UBVRIZ/JHK bandpasses via aperture photometry, and additionally their fluxes in each redshift bin are combined in an unweighted average to yield a single averaged SED for each redshift range. These average fluxes for redshift binned sBzKs in each UV-radio waveband are indicated in Table 2. IR data in the ECDF-S is available in IRAC bands at 3.6, 4.5, 5.8 and $8.0 \mu\text{m}$ (SIMPLE; Damen et al. 2010). As discussed in Section 2, IRAC data were used in photometric redshift determination; however, these data were not used in the fits to determine L_{IR} .

MIPS 24, 70 μm . Infrared data were obtained from the *Spitzer Space Telescope* Multi Band Imaging Photometer (MIPS) 24 μm and 70 μm images that reach 5σ depths of $50 \mu\text{Jy}$ and 3 mJy , respectively (FIDEL, Dickinson et al. in prep). K band sBzK positions are compared to the 24 μm (70 μm) catalog, with positions less than $2''$ ($4''$) separation as the criterion for individual detection in each MIPS band, respectively. Individual detections are removed from the list for stacking. In 24 μm data, in redshift bins from $0.9 < z \leq 1.2$, $1.2 < z \leq 1.5$, $1.5 < z \leq 2.0$ and $2.0 < z \leq 3.2$, there are 8, 65, 98, 68 individual detections and 41, 89, 122 and 81 stacked positions, respectively. Similarly, in 70 μm data, in these same redshift bins, there are 2, 6, 11, 3 individual detections and 47, 147, 209, 146 stacked positions. Stacking is performed on a residual image, after removing the matched sources from the list, as summarized in Huynh et al. (2007). The stacking algorithm computes an inverse variance weighted average of the flux at each stack position. We use an ordinary average of the individual detections and the stacking detection to yield a single combined estimate for the flux of each set of galaxies. We show in Section 8 that, although the difference between these two approaches is small, the ordinary average

is preferred because the weighted average can introduce a bias to the combined flux estimate.

BLAST 250, 350, 500 μm . Submillimeter data at 250, 350, 500 μm were obtained from the public archive of the Balloon-borne Large Area Space Telescope (BLAST) survey of the ECDF-S, which reaches 1σ depths of 36, 31, 20 mJy at 250, 350 and 500 μm , respectively, in an 8.7 deg² wide field and 1σ depths of 11, 9, 6 mJy at 250, 350, 500 μm in a 0.8 deg² deep field (Devlin et al. 2009).

The redshift binned sBzKs are stacked in the public BLAST ‘smooth’ data (variance-weighted correlation between the signal maps and the effective point-spread functions). Each pixel in these data products represented the maximum likelihood flux density (Jy) of an isolated point source centered over the pixel (Truch et al. 2008).

We use an improved submillimeter stacking and deblending algorithm for stacking in 250, 350, 500 and 870 μm data that deals effectively with the problem of confusion (Kurczynski & Gawiser 2010). Confusion severely limits the effectiveness of stacking in deep surveys with limited angular resolution (Condon 1974; Hogg 2001), particularly at far IR-submillimeter wavelengths, and causes a bias in stacking results. Deblending corrects measured fluxes for confusion from these adjacent sources. This stacking and deblending algorithm greatly reduces bias in the flux estimate with nearly minimum variance. For more details, see Kurczynski & Gawiser (2010). All galaxies in the MUSYC catalog with $K_{AB} < 22$ are used in the deblending calculations.

We find stacking detections (defined as $\text{SNR} \geq 3$) in the 250 μm data for the redshift bin $1.5 < z \leq 2.0$ (stacking detection $\text{SNR} = 12$), and in the 350 μm data for the redshift bins $1.2 < z \leq 1.5$ ($\text{SNR} = 3$) and $1.5 < z \leq 2.0$ ($\text{SNR}=10$), and in the 500 μm data, for the redshift bin $1.5 < z \leq 2.0$ ($\text{SNR}=10$). See Table 2 for the stacked flux densities and errors in each waveband. In the SED fits discussed below, the measured fluxes of formal non-detections and their appropriate error bars are included in the fits. Combining all of the BzK galaxies, without regard to redshift binning, yields stacking detections in 250, 350, 500 μm data of 3.9 ± 0.4 mJy, 2.5 ± 0.3 mJy, 1.8 ± 0.2 mJy respectively. Fluxes reported from stacking BzK galaxies in the same field, selected from a different K band catalog, with a different stacking algorithm are larger by about a factor of two than those values presented here (Marsden et al. 2009). In addition to the differences in sample and stacking algorithm, another source of this discrepancy may be the exclusion of X-ray detected sources (AGN) in the present work.

LESS 870 μm . Submillimeter data at 870 μm were obtained from the Large Apex Bolometer Camera ECDF-S Submillimeter Survey (LESS) (Weiss et al. 2009), which reaches a 1σ depth of approximately 1.2 mJy beam⁻¹. The LESS catalog contains 126 individually detected submillimeter sources (Weiss et al. 2009) and these data have been used previously for stacking analyses of BzK galaxies (Greve et al. 2010).

K band sBzK positions are compared to the 870 μm catalog to determine individual detections. In 870 μm data, in redshift bins from $0.9 < z \leq 1.2$, $1.2 < z \leq 1.5$, $1.5 < z \leq 2.0$ and $2.0 < z \leq 3.2$, there are 1, 3, 12, 5 individual detections and 49, 155, 218, 147 stacked positions, respectively. The simultaneous stacking and deblending

algorithm discussed above is used to stack positions in the final, LESS beam smoothed flux map (Weiss et al. 2009). All galaxies in the MUSYC K band catalog are used in the deblending calculations. Individual detections and the stacking detections are combined into a single average signal for each redshift bin, as discussed above and in Section 8. We find significant stacking detections in all but the lowest redshift bin, see Table 2. An average detection for the entire sample, $0.9 < z \leq 3.2$, yields 0.49 ± 0.05 mJy ($\text{SNR}=10$), consistent with the results of Greve et al. (2010) for a nearly identical set of galaxies in the same field.

Radio. Radio data at 610 MHz were obtained from the Giant Metrewave Radio Telescope (GMRT) survey of the ECDF-S, which reaches a typical depth of 40 $\mu\text{Jy beam}^{-1}$ (Ivison et al. 2010a). 1.4 GHz data were obtained from the Very Large Array (VLA) survey, which covers the ECDF-S to a typical depth of 8 $\mu\text{Jy beam}^{-1}$ and includes 464 cataloged sources (Miller et al. 2008). In the radio regime we adopted the technique of Ivison et al. (2007) - dividing the catalog into the same redshift bins used earlier. Median images are made from the VLA and GMRT stacks, to reduce the influence of radio-loud AGN. In the radio regime, where the spatial resolution is relatively high, making images allows us to conserve flux density that would otherwise be lost due to smearing by astrometric uncertainties and finite bandwidth (chromatic aberration) at the cost of larger flux density uncertainties. Total flux densities are measured within *AIPS* using Gaussian fits over 9×9 -pixel regions; we determine the appropriate source centroid by making radio stacks using every available sBzK galaxy, then use this centroid to minimize flux density uncertainties and avoid spurious fits; at 1.4 GHz, where both forms of smearing are most prevalent, flux densities are 1.37 and $1.55 \times$ higher than the peak values at 610 MHz and 1.4 GHz, respectively. Such losses are not expected where the astrometry is accurate to a small fraction of a beam, as it is in far-IR and submillimeter regimes. Radio fluxes are indicated in Table 2 and discussed below.

X-ray. X-ray exposure in the ECDF-S consists of 4 Ms in the central $\approx 16' \times 16'$ Chandra Deep Field - South, reaching approximate sensitivities of 1×10^{-17} and 7×10^{-17} erg cm⁻² s⁻¹ in the 0.5-2.0 and 2.0-8 keV bands, respectively, and giving this field the deepest X-ray coverage to date.¹³ These data are augmented with 4 flanking 250 ks exposures that complete the $\approx 30' \times 30'$ ECDF-S field, and reach sensitivity limits of 1.7×10^{-16} and 3.9×10^{-16} erg cm⁻² s⁻¹ in the 0.5-2.0 and 2.0-8.0 keV bands, respectively (Lehmer et al. 2005; Virani et al. 2006).

To make optimum use of the 4 Ms data in the CDF-S, X-ray stacking analysis was performed only for sources in this region. A position dependent aperture correction was used to account for the varying Chandra PSF with off-axis angle, and to minimize this correction, only sources within 10' of the aim point were stacked. Sources that have an X-ray detection closer than 15'' to the stacking position are removed to provide a better estimation of the background. This procedure leaves 12, 29, 50, 31 source positions in redshift bins from $0.9 < z \leq 1.2$,

¹³ Sensitivity estimates are based upon the 2Ms data; a catalog of the 4Ms data set has not yet been released.

$1.2 < z \leq 1.5$, $1.5 < z \leq 2.0$ and $2.0 < z \leq 3.2$ respectively that are stacked in *Chandra* soft band and hard band data.

Background subtracted counts are converted to flux density by assuming a power law photon spectrum index, $\Gamma = 1.2$, and cut off energy $E_c = 20$ keV. This spectrum slope is consistent with the observed spectrum of High-Mass X-ray Binaries (HMXBs; Lutovinov et al. 2005), that are expected to dominate the X-ray emission from star-forming galaxies, e.g. (Persic & Rephaeli 2002). This choice of assumed spectrum is discussed further in Section 4.4.

4. METHOD OF ESTIMATING LUMINOSITIES AND STAR FORMATION RATES

The multiwavelength, stacked flux densities discussed in Section 3 are used to form spectral energy distributions (SEDs) for the sBzK galaxies in our four redshift bins. In particular, the IR-submillimeter SEDs are used to estimate IR luminosity and the corresponding SFR for each bin. To compare different SFR calibrations, we also compute UV, X-ray and radio luminosities from these data.

4.1. IR Luminosity and SFR Estimation

In order to estimate L_{IR} , we fit observed IR photometry to template libraries from Chary & Elbaz (2001), hereafter CE01. These templates are based on the stellar population synthesis models of Silva et al. (1998), which employ Simple Stellar Populations (SSP) of varying age and metallicity and include enrichment of the interstellar medium by outflows from Asymptotic Giant Branch (AGB) stars. The templates are formed by interpolation of the SEDs of several prototypical galaxies in the local universe representing luminosity classes of normal galaxies (M51), starburst galaxies (M82), luminous infrared galaxies, LIRGs (NGC 6090), and ultraluminous infrared galaxies, ULIRGs (Arp 220). Template SEDs are generated in the range $0.1\text{--}1000\ \mu\text{m}$; however, the optical-NIR spectral regions of the templates are considered to be highly uncertain. Symeonidis et al. (2008) compare and contrast various other commonly used template sets.

Estimation of L_{IR} from IR data has often been complicated by the availability of only a single IR photometric measurement, most commonly observed frame $24\ \mu\text{m}$, thereby making the resulting fits highly uncertain. For $z \sim 2$ systems, observed frame $24\ \mu\text{m}$ corresponds to a rest frame wavelength regime dominated by spectral emission features of Polycyclic Aromatic Hydrocarbons (PAHs) and hot dust from AGN and silicate absorption. PAHs are honeycombed, carbon ring molecules that reprocess UV starlight and give rise to ubiquitous mid-IR spectral lines observed in many astrophysical systems (Tielens 2008); however, these features are not necessarily ideal proxies for star formation in the local universe (Peeters et al. 2004), and they further complicate SED fitting of high redshift systems.

In this investigation, we explore several approaches to fitting the IR-radio data to CE01 templates to determine L_{IR} . In each case, a region of the IR-radio spectrum is chosen for template fitting. Fits are performed on each photometric redshift bin averaged spectrum. The template rest frame luminosity is converted to an observed frame flux distribution at the median redshift of

the redshift bin. Then the observed frame model flux distribution is convolved with each photometric band-pass transmission function to generate predicted model photometry. The predicted photometry is combined with observed photometric fluxes and errors to generate a χ^2 statistic for each fit. Each template in the library is fit in this way, with the smallest χ^2 fit chosen as the best fit template. For fits that include observations at multiple wavelengths, an overall normalization, A , set to its analytical best fit value via $\partial\chi^2/\partial A = 0$, is factored into the best fit spectrum.

Uncertainties in L_{IR} are determined from 68% confidence intervals determined from variations in χ^2 with normalization. We considered separately the effects of error in the redshift. We approximate the error of the median redshift by computing the error of the mean of individual redshifts, whose errors are given by $\delta z/(1+z) = 0.009$ (Cardamone et al. 2010). This error of the mean diminishes according to $1/\sqrt{N}$, where N is the number of objects in each redshift bin. We computed L_{IR} for our samples at the $\pm 1\sigma$ values of the mean redshift and found the results to be the same as the actual L_{IR} to within the normalization error. Consequently, the error in the mean redshift does not contribute significantly to the overall L_{IR} uncertainty. Because the median redshift is more robust to the presence of outliers, we consider the error of the mean to be an upper bound to the error of the median. We also address the effect of redshift errors via simulations, as discussed in Section 4.5. On this basis, we ignore error of the median redshift in subsequent calculations.

To compare the multiwavelength approach to a single band L_{IR} estimate, we also perform fits to the $24\ \mu\text{m}$ data alone. For these single band fits, there is no free normalization factor, and the CE01 template luminosity is used directly to estimate L_{IR} . For the single band fits, the variation of χ^2 with template index is used as the basis for determining confidence intervals; 68% error bars are found for the L_{IR} estimate, and these errors are propagated into an SFR uncertainty. We explore several additional approaches to estimating L_{IR} from the data using CE01 template fits: For each redshift bin, we fit (i) the entire optical through radio data, (ii) the $24\ \mu\text{m}$ and longer wavelength data, (iii) the long wavelength IR and radio data excluding $24\ \mu\text{m}$, (iv) only the submillimeter data near the peak of the dust emission spectrum, and (v) the IR data excluding the radio data. We also fit models of gray body emission. Some of these fits are illustrated in Table 3 and Figure 4 and are discussed in Section 5.

We use the calibration of Kennicutt (1998b) to convert L_{IR} to estimated star formation rate. This calibration is based on the starburst synthesis models of Leitherer & Heckman (1995), and it assumes a continuous burst of age 10-100 Myr, solar abundances, Salpeter IMF, and bolometric luminosity arising from dust reradiation. This calibration relates the L_{IR} integrated from $8\text{--}1000\ \mu\text{m}$ to star formation rate according to

$$SFR_{IR}(M_{\odot}\ \text{yr}^{-1}) = 4.5 \times 10^{-44} L_{IR}(\text{erg}\ \text{s}^{-1}) \quad (2)$$

The uncertainty in this relation arises from uncertainties in L_{IR} of their original sample, confounding sources of IR emission in their sample, and the use of a fixed con-

tinuous burst model; the combined errors in the SFR are estimated as being a factor of $\sim 2 - 3$. This systematic uncertainty in luminosity to SFR conversion dominates the overall error budget in SFR estimates; the impact of this substantial systematic uncertainty on other SFR estimates, many of which depend indirectly on the L_{IR} -SFR relationship, is discussed in Section 6.1. SFR estimates for our redshift binned sBzKs are discussed in Section 5.1. Uncertainties in these SFR estimates include only errors in L_{IR} (arising from photometry, and template normalization).

4.2. UV Continuum Luminosity and SFR Estimation

To determine UV continuum luminosity before dust correction, L_{ν}^{Uncorr} , we use the available optical-NIR photometry. We estimate the rest frame 1600 Å flux density, f_{ν}^{Uncorr} , via interpolation of the two bracketing broad band fluxes. The specific luminosity at 1500 Å, L_{ν}^{Uncorr} in units of $\text{erg s}^{-1} \text{Hz}^{-1}$, at the redshift, z , is then found from the flux density, f_{ν}^{Uncorr} in units of μJy and the luminosity distance, D_L , according to

$$L_{\nu}^{Uncorr} = 1 \times 10^{-29} f_{\nu}^{Uncorr} \frac{4\pi D_L^2}{(1+z)}. \quad (3)$$

To convert luminosity to SFR, we use the calibration of Kennicutt (1998a), which corresponds to the calibration of Madau et al. (1998) converted to Salpeter IMF and 0.1 – 100 M_{\odot} mass limits.

$$SFR_{UV}(M_{\odot} \text{ yr}^{-1}) = 1.4 \times 10^{-28} L_{\nu}(\text{erg s}^{-1} \text{Hz}^{-1}) \quad (4)$$

This calibration assumes continuous star formation over time scales of 10^8 years or longer. Kennicutt (1998a) discusses sources of systematic uncertainty in the various published L_{ν} – SFR calibrations as arising from the use of different stellar libraries and assumptions about the star formation time scales; the published calibrations differ by about a factor of 2. We use Equation 4 to compute SFR from uncorrected luminosities, L_{ν}^{Uncorr} , to estimate the contribution to SFR that is unobscured by dust. We also apply this expression to dust corrected luminosities to determine dust corrected UV SFR, SFR_{UV}^{Corr} , as discussed below.

Dust absorption causes reddening of the spectrum since shorter wavelengths are preferentially absorbed. As a result, it is reasonable that dust radiation, quantified by the ratio of integrated IR to UV luminosity, $IRX \equiv L_{IR}/L_{UV}$, is found to be correlated with the UV spectral index, β , where $f_{\lambda} \propto \lambda^{\beta}$ when calibrated using starburst galaxies in the local universe (Meurer et al. 1999). This correlation has been used to correct UV SFR estimates for dust attenuation in high redshift LBGs, (e.g. Meurer et al. 1999; Adelberger & Steidel 2000; Reddy et al. 2010), BzK galaxies (Daddi et al. 2007b), and galaxies at lower redshift (e.g. Buat et al. 2010; Howell et al. 2010; Takeuchi et al. 2010).

In order to compute this dust correction, we fit the rest frame UV f_{λ} spectrum to a power law: $f_{\lambda}(\lambda) = A\lambda^{\beta}$. We use a range of trial β values: $-2.5 < \beta < 1.0$ in steps $\Delta\beta = 0.01$. The wavelength range of the fits, [1268, 2580] Å in the rest frame, are chosen to be the same as that used in Calzetti et al. (1994), which Meurer et al. (1999) also

adopted. These values are redshifted into the observed frame, and photometry data falling within this range are used for the fits. For each trial value of β , predicted flux values are computed at each relevant, observed wavelength by integrating over the filter bandpass transmission function, $T(\lambda)$, and IGM absorption function, $M(\lambda)$, from Madau (1995). The integral is expressed in terms of the number of photons detected, hence an extra factor of λ is included in the integrand, as illustrated below in Equation 5. The integral is normalized to units of μJy by dividing by the corresponding integral of a flat in f_{ν} reference spectrum ($f_{\nu}^{ref} = 1 \mu\text{Jy}$), which is converted to a photon number spectrum. This approach leads to the expression for predicted flux density, $f_{\nu_i}^{pred}$, for each broadband filter, i

$$f_{\nu_i}^{pred}(\mu\text{Jy}) = A \frac{\int \lambda^{\beta} T_i(\lambda) M(\lambda) \lambda d\lambda}{\int f_{\nu}^{ref}(\lambda) T(\lambda) \lambda d\lambda} \quad (5)$$

The statistic X^2 is formed as a summation over the observed photometric data, $f_{\nu_i}^{obs}$, with errors, σ_i^{obs} , taken from the data.¹⁴

$$X^2 = \sum_i \left(\frac{f_{\nu_i}^{obs} - f_{\nu_i}^{pred}}{\sigma_i^{obs}} \right)^2 \quad (6)$$

We optimize the normalization parameter, A , by selecting the value for which $\partial X^2 / \partial A = 0$. Finally the complete, normalized predicted flux in μJy is computed from Equation 5. The above fit procedure is repeated for each trial β value, and the fit with the smallest X^2 is chosen to represent the data.

The resulting power law index, β , is then used to compute the UV extinction from the empirical relation of Meurer et al. (1999)

$$A_{1600} = 4.43 + 1.99\beta, \quad (7)$$

which is found to have 0.55 mag dispersion about their fit in A_{1600} and a standard error in the fit zero point of 0.08 mag; see Equation (11) and Figure 1 from Meurer et al. (1999). The UV extinction is then used to correct the measured UV flux according to

$$F_{UV}^{Corr} = 10^{0.4A_{1600}} F_{UV}^{Uncorr} \quad (8)$$

Finally the corrected UV flux is used to estimate the star formation rate using Equation 4. The above procedure is executed for each sBzK galaxy individually as well as for the unweighted average spectrum of all sBzKs within a redshift bin, whereby the bin median redshift is used to compute the luminosity distance.

Uncertainties to the corrected UV luminosity arise from observed flux uncertainty, error in the dust correction factor, and photometric redshift error (for individual galaxies, we adopt the value of $\delta z / (1+z) = 0.009$; for the average spectra, this contribution is negligible, as discussed in Section 4.1 and via simulations in Section 4.5). These uncertainties are combined using standard error analysis. We do not include the systematic uncertainty associated with the luminosity – SFR calibration

¹⁴ since each observed flux value is a weighted average of many observations, the observed errors are very small; due to systematics in the photometry, the resulting X^2 values are very large compared to a χ^2 statistic

(discussed above, about a factor of 2); rather we consider this uncertainty with similar systematics from other waveband estimators separately in Section 6.1. The results of these computations are shown in Table 4 and discussed in Section 5.2.

4.3. Radio Luminosity and SFR Estimation

Our data include flux measurements, S_ν , at 1.4 GHz and 610 MHz for each of the redshift binned spectral energy distributions; we estimate the radio spectral index, $S_\nu \propto \nu^\alpha$, (typical $\alpha \sim -0.8$ for star forming galaxies, e.g. Condon 1992) from these two measurements. In estimating radio luminosity, we use the flux estimates obtained from median stacking of galaxies in each of the redshift bins to obtain results that are robust against radio bright outliers (caused by radio lobes from recent AGN activity that X rays will not always detect). We use the median redshift, z , and the corresponding luminosity distance, D_L , in Mpc to compute the aggregate rest frame 1.4 GHz luminosity, $L_{\nu,1.4GHz}$ in units of W Hz^{-1} , from the observed frame 1.4 GHz flux, S_ν , in units of μJy according to

$$L_{\nu,1.4GHz} = 9.523 \times 10^{12} \frac{4\pi D_L^2}{(1+z)^{1+\alpha}} S_{\nu,1.4GHz} \quad (9)$$

We assume here that the distribution of galaxies in flux is independent of redshift across a bin. This assumption would be violated in the case of source evolution within a bin, so the subsequent SFR estimates should be interpreted with some caution.

To estimate star formation rate from $L_{\nu,1.4GHz}$, we use the model of Condon (1992) as implemented in Haarsma et al. (2000) and Dunne et al. (2009) with the exception that we use spectral indices, α , determined from the data rather than using the typical value of $\alpha = -0.8$. Following the implementation in Haarsma et al. (2000), SFR in units of $M_\odot \text{ yr}^{-1}$ is a function of frequency in units of GHz, $L_{\nu,1.4GHz}$ in units of W Hz^{-1} , scaled by a factor Q and is given by

$$\text{SFR}_{1.4GHz}^{\text{Condon}} = Q \frac{L_{\nu,1.4GHz}}{5.3 \times 10^{21} \nu^\alpha + 5.5 \times 10^{20} \nu^{-0.1}} \quad (10)$$

We use the value $Q = 5.5$ to scale the $\text{SFR}(M > 5 M_\odot)$ calculated in Condon (1992) to $\text{SFR}(0.1-100 M_\odot)$ used here; this scaling factor depends on the assumed (Salpeter) IMF used here and by Haarsma et al. (2000).

For comparison, we also estimate SFR from 1.4 GHz flux using the calibration of Bell (2003). This calibration is based on the IR-radio correlation; it assumes that nonthermal radio emission directly tracks the SFR, and is chosen so the radio SFR matches the IR SFR for $L \geq L^*$ galaxies. The SFR calibration

$$\text{SFR}_{1.4GHz}^{\text{Bell}} (M_\odot \text{ yr}^{-1}) = 5.52 \times 10^{-22} L_{1.4GHz} \quad (11)$$

is adopted here. A similar calibration is found in Yun et al. (2001). $\text{SFR}_{1.4GHz}^{\text{Condon}}$ exceeds $\text{SFR}_{1.4GHz}^{\text{Bell}}$ by a factor of two; the calibration of Condon (1992) explicitly models the thermal and nonthermal emission mechanisms, whereas the calibration of Bell (2003) relies upon the IR-Radio correlation. Thus we expect agreement between $\text{SFR}_{1.4GHz}^{\text{Bell}}$ and IR based SFR estimates, if the IR-radio correlation continues to hold at high redshift,

as has indeed been suggested by recent *Herschel Space Observatory* observations (Ivison et al. 2010b; Sargent et al. 2010).

Uncertainties to the radio luminosities are computed by incorporating uncertainties from redshift, spectral index and flux measurement; these uncertainties are propagated into the SFR uncertainties. When only flux measurement uncertainties are included in the error budget, uncertainties in $\text{SFR}_{1.4GHz}^{\text{Condon}}$ agree to within 30% of published values (Dunne et al. 2009). However, when spectral index estimate uncertainties are included, the total SFR uncertainties are substantially larger than previously reported values. In the calibration of Bell (2003), scatter in the IR-radio correlation contributes a factor of 1.8 (dispersion of 0.26 dex for individual galaxies) to the uncertainty and dominates the total error budget; this uncertainty is combined in quadrature with the luminosity uncertainty to yield the total SFR uncertainty. Results of these computations are shown in Table 5 and discussed in Section 5.3. Additional systematic uncertainty arising from the L_{IR} -SFR calibration is discussed in Section 6.1

4.4. X-Ray Luminosity and SFR Estimation

Rest frame luminosity estimates for our sBzK galaxies in each photometric redshift bin are obtained using the median redshifts to determine luminosity distance. The observed frame soft band fluxes are converted to rest-frame 2-10 keV luminosities assuming a spectrum with photon index $\Gamma=1.2$ and cut off energy, $E_c=20$ keV. The rest frame 2-10 keV luminosities are used to estimate SFR.

As shown by Persic & Rephaeli (2002), the X-ray spectrum of star-forming galaxies that do not have an AGN is dominated by HMXBs, which are best described by $\Gamma = 1.2$ and a cutoff energy of 20 keV. Many star-forming galaxies also present a thermal component, which is typically softer in X-rays with $kT \sim 0.7$ keV. The spectrum of the resulting combination is something softer than a pure $\Gamma = 1.2$, but not quite $\Gamma = 2$. In studying Lyman Break Galaxies, Nandra et al. (2002) assumed an intrinsic spectrum of $\Gamma = 2.0$, more typical of local Seyfert galaxies and soft X-ray selected quasars. To estimate the effect of different assumptions of photon spectrum index, we also computed counts to flux and luminosity conversions using $\Gamma = 1.9$. The differences of conversions from counts to flux are $\sim 11\%$. Similarly, the differences in conversion from observed frame soft band to rest frame hard band are $\sim 16\%$. Thus in the soft band, the uncertainties due to an assumed spectral shape are $\sim 20\%$. X-ray fluxes, luminosities and SFRs are tabulated in Table 6 and discussed in Section 5.4.

Non AGN X-ray emission from galaxies originates from X-ray binaries, supernovae, supernova remnants and O stars (e.g. Fabbiano 2006; Brandt & Hasinger 2005). Total X-ray luminosity has been found to be correlated with radio (e.g. Bauer et al. 2002) and IR luminosity (e.g. Ranalli et al. 2003) leading to an X-ray SFR correlation. The calibration of Ranalli et al. (2003) is widely used, and it is based upon the X-ray - IR luminosity correlation observed in galaxies with $L_{2-10\text{keV}} \lesssim 10^{41} \text{ erg s}^{-1}$. The SFR in units of $M_\odot \text{ yr}^{-1}$ is related to the 2-10 keV

luminosity, $L_{2-10\text{keV}}$ in units of erg s^{-1} , according to

$$SFR_{2-10\text{keV}}^{\text{Ranalli}} = 2.0 \times 10^{-40} L_{2-10\text{keV}}. \quad (12)$$

This calibration implicitly assumes the L_{IR} -SFR calibration of Kennicutt (1998a) and a Salpeter IMF (0.1-100 M_{\odot}) consistent with other calibrations mentioned in this paper.¹⁵ However, the Ranalli et al. (2003) sample includes few star forming galaxies in the ULIRG regime, where the L_X - SFR correlation is observed to drop (Lehmer 2010).

The uncertainty to $SFR_{2-10\text{keV}}^{\text{Ranalli}}$ is computed by adding in quadrature uncertainties in X-ray luminosity and the 0.09 dex error of the slope in the X-ray - IR luminosity correlation (see Ranalli et al. (2003) Eq. 10). Luminosity uncertainties are computed by propagating the flux estimate errors; redshift errors of the average spectrum can be neglected, as discussed in Section 4.1 and shown in simulations discussed in Section 4.5.

Instantaneous SFRs are found to be correlated specifically to luminosity from short lived High Mass X-ray Binaries (HMXBs; e.g. Grimm et al. 2003; Colbert et al. 2004; Persic et al. 2004) while slowly evolving, Low Mass X-ray Binaries (LMXBs) are linked to stellar mass (Colbert et al. 2004), i.e. integrated SFR. The X-ray SFR calibration of Persic et al. (2004) is therefore based upon the luminosity of HMXBs, and it relates SFR in units of $M_{\odot} \text{ yr}^{-1}$ to the 2-10 keV HMXB luminosity, $L_{2-10\text{keV}}^{\text{HMXB}}$ in units of erg s^{-1} , according to

$$SFR_{2-10\text{keV}}^{\text{Persic}} = 10^{-39} L_{2-10\text{keV}}^{\text{HMXB}}. \quad (13)$$

The fraction, f , of HMXB X-ray luminosity to total X-ray luminosity has been estimated as $f \sim 0.2$ (with substantial scatter due to low statistics) for nearby star forming galaxies (Persic et al. 2004) and for high redshift ($z > 1$) galaxies, in the absence of definitive estimates from X-ray spectroscopy, the value $f = 1$ has been used on the assumption that LMXBs (or other sources of emission) contribute a negligible fraction to the total X-ray luminosity at $z \sim 2$ (Persic et al. 2004; Persic & Rephaeli 2007).

Assuming $f = 0.2$ for nearby star forming galaxies leads to $L_{2-10\text{keV}}^{\text{HMXB}} = 0.2 L_{2-10\text{keV}}^{\text{Total}}$, which brings the calibration of Persic et al. (2004) into equivalence with the calibration of Ranalli et al. (2003). Our data for high redshift galaxies do not directly constrain the HMXB luminosity fraction; with the assumption $f = 1$, $L_{2-10\text{keV}}^{\text{HMXB}} = L_{2-10\text{keV}}^{\text{Total}}$, and the SFRs estimated from Persic et al. (2004) exceed those of Ranalli et al. (2003) by a factor of 5. In computing SFR, we adopt $f = 1$ for the X-ray calibration of Persic et al. (2004) for our sample of sBzKs, and we regard the resulting SFRs as upper limits.

The relative contribution of LMXBs to the total X-ray luminosity is believed to decline above $z \sim 1$ (Ghosh & White 2001), and to be subdominant in high SFR (e.g. $> 100 M_{\odot} \text{ yr}^{-1}$) galaxies. A bilinear relation between X-ray luminosity and both SFR and stellar mass, M_{\star} , has been proposed, (e.g. Colbert et al. 2004). The X-ray

SFR calibration of Lehmer et al. (2010) is derived from such a relationship

$$L_{2-10\text{keV}}^{\text{Lehmer}} = \alpha M_{\star} + \beta SFR. \quad (14)$$

In analysis of LIRGs/ULIRGs extending to $L_{2-10\text{keV}} \sim 10^{41.5} \text{ erg s}^{-1}$, Lehmer et al. (2010) report $\alpha = (9.05 \pm 0.37) \times 10^{28} \text{ erg s}^{-1} M_{\odot}^{-1}$ and $\beta = (1.62 \pm 0.22) \times 10^{39} \text{ erg s}^{-1} (M_{\odot} \text{ yr}^{-1})^{-1}$. In the absence of the M_{\star} term in Equation 14, and with the assumption $f = 1$, as discussed above, this calibration becomes consistent to within errors of the calibration of Persic et al. (2004), after accounting for the differences in IMF assumed by these authors.

In order to compute $SFR_{2-10\text{keV}}^{\text{Lehmer}}$, we estimate stellar masses for our redshift binned sBzK samples. We use the empirical correlation between observed frame K band magnitude and stellar mass for sBzKs at $z > 1.4$, determined from SED fits, that is presented in Daddi et al. (2004).

$$\log(M_{\star}/10^{11} M_{\odot}) = -0.4(K^{\text{tot}} - K^{11}) \quad (15)$$

$K^{11} = 21.4$ is the K band magnitude corresponding on average to a stellar mass of $10^{11} M_{\odot}$. Daddi et al. (2004) report uncertainties of $\sim 40\%$ with this relation, which is sufficient for our purpose of estimating SFRs because the stellar mass component to $L_{2-10\text{keV}}$ is subdominant for our sample of sBzKs (see Kannappan & Gawiser (2007) for a full discussion of stellar mass uncertainties).

Uncertainties in $SFR_{2-10\text{keV}}^{\text{Lehmer}}$ are calculated by propagating the uncertainties in the luminosity and stellar mass, along with the reported uncertainties in the parameters α and β indicated above. This calibration is based implicitly on the L_{IR} -SFR calibration of Bell et al. (2005) which yields lower SFRs by $\approx 13\%$ compared to the corresponding calibration of Kennicutt (1998b); however, we neglect this small calibration difference, and discuss systematic uncertainties in comparison with other SFR indicators in Section 6.1.

4.5. SIMULATIONS

The approach to stacking presented here consists of combining galaxies in bins of photometric redshift, in order to study star formation in sBzK galaxies over cosmic time. Averaging the photometric flux density from galaxies at slightly different redshifts introduces redshift smearing. In order to study this effect, we simulate a set of identical CE01 template spectral models. These spectra are shifted to the identical redshifts of galaxies in our $1.5 < z \leq 2.0$ redshift bin, and then averaged together, analogous to the actual stacking procedure. The redshift bin averaged spectrum is nearly identical to the template spectrum except for moderate smearing of the emission peaks that contributed a negligible amount to the integral; consequently, the quantity of interest, the integrated IR luminosity, is robust against redshift smearing over our bin widths.

Of greater concern is the effect on L_{IR} due to photometric redshift errors. To quantify the contribution of these errors to the estimated L_{IR} for each redshift bin, we simulate a set of identical CE01 template sources, with spectra equal to the best fit spectrum. These sources are distributed in redshift to simulate the observed source

¹⁵ Note that the radio SFR calibration cited in Ranalli et al. (2003) refers to $M > 5 M_{\odot}$ mass range. For a Salpeter IMF, the resulting X-ray-radio derived SFRs differ by a factor of 5.5 from the 0.1-100 M_{\odot} range used here.

distribution and to account for photometric redshift errors. The photometric redshift error distribution is determined from comparison of spectroscopic and photometric redshifts for the subset of sources with both estimates available and is shown in Figure 3. This distribution is well fit by a Gaussian with mean = -0.021 (i.e. bias) and $\sigma=0.081$ (i.e. scatter). The bias is first removed from the simulated object redshifts, and then artificial redshift errors drawn from this biased, Gaussian distribution are added in each repeated trial of the simulation. The resulting spectra are averaged, and this averaged spectrum is integrated to determine L_{IR} . An example of these spectra from the $1.5 < z \leq 2.0$ redshift bin simulation is illustrated in Figure 5. From the figure, it is apparent that the averaged spectrum has a slightly higher flux than the single object spectrum near the emission peak and therefore will overestimate L_{IR} . For each repeated trial, the fractional error in the L_{IR} estimate is determined by comparing the bin averaged L_{IR} to the corresponding quantity determined from integrating the single CE01 template at the bin median redshift. The frequency distribution of L_{IR} fractional errors is determined directly from 10^3 repeated trials for each redshift bin. The fractional error distributions for redshift bins $0.9 < z \leq 1.2$, $1.2 < z \leq 1.5$, $1.5 < z \leq 2.0$ and $2.0 < z \leq 3.2$ are each Gaussian with mean = 16%, 10%, 14%, 5% and $\sigma = 7\%$, 3%, 3%, 3% respectively. The fractional error distribution for the $1.5 < z \leq 2.0$ bin is illustrated in Figure 5.

5. RESULTS

5.1. IR SFR Estimates

SFR_{IR} values are obtained from CE01 template fits to determine the integrated IR luminosity. We tried various approaches to fitting the IR-radio data to CE01 and gray body templates, as illustrated in Figure 4 and Table 3. The low redshift bin, $0.9 < z \leq 1.2$, suffers from lack of detections in the BLAST sub-millimeter bands (upper 1σ error bars are shown in the figure). Data in the highest redshift bin, $2.0 < z \leq 3.2$, also suffer from weak sub-millimeter detections, leading to large error bars and poor fits. Redshift binned spectra in the range $1.2 < z \leq 1.5$ and $1.5 < z \leq 2.0$ include significant submillimeter detections in BLAST and LESS bands. In general, optical/NIR data are excluded from the fits to CE01 templates because the templates are considered to be incomplete for $\lambda < 1\mu\text{m}$.

We adopt CE01 template fits in the range $\lambda \geq 24\mu\text{m}$ for our preferred L_{IR} values. Though not formally the best χ^2 , they are comparable to the best fits (e.g. $\chi^2_\nu = 2$ for $\lambda \geq 24\mu\text{m}$ vs $\chi^2_\nu = 0.77$ for $\lambda > 24\mu\text{m}$ in the $1.2 < z \leq 1.5$ bin) and including the $24\mu\text{m}$ photometry makes maximum use of the available data. Furthermore, these fits better match the data outside the fitting region than the $\lambda > 24\mu\text{m}$ fits.

For comparison with a complementary method of L_{IR} estimation, each plot of Figure 4 illustrates fits of the submillimeter peak (70-870 μm data only) to a gray body spectrum, $S_\nu \propto \nu^\beta B(\nu, T)$ where the emissivity index, $\beta = 1.5$, and $B(\nu, T)$ is the Planck function. For the redshift range $0.9 < z \leq 1.2$, the temperature is fixed at 50 K, which gives a better visual fit to the emission peak than lower temperatures used in other redshift bins,

and only the normalization is allowed to vary. For the redshift range $1.2 < z \leq 1.5$ (second row from the top), the gray body fit has χ^2 and L_{IR} values similar to the best fit CE01 template; the best fit temperature is 41 ± 5 K. The gray body fit to the next highest redshift bin, $1.5 < z \leq 2.0$, yields a dust temperature of 43 ± 5 K. For the redshift range $2.0 < z \leq 3.2$, the temperature is fixed at 40 K and the normalization is allowed to vary.

L_{IR} values obtained from Table 3 are consistent with other results in the literature for BzKs. Daddi et al. (2005) select BzKs to the same depth in K band as presented here, and use MIPS $24\mu\text{m}$ photometry to estimate $L_{IR} \sim 1.7 \times 10^{12} \text{ erg s}^{-1}$ for BzKs in the range $1.4 < z < 2.5$. Murphy et al. (2009) find L_{IR} values in the range $10^{11-12} L_\odot$ for their sample of 22 BzKs studied with *Spitzer* mid-IR spectroscopy and broad band FIR-submillimeter SED fits.

5.2. UV SFR Estimates

As discussed in Section 4.2, we compute UV SFRs for individual sBzK galaxies in each redshift bin. Table 4 illustrates the unweighted averages of fit results for each redshift bin. Averages excluded galaxies with poor fits to the spectral index, β , identified by large χ^2 and/or best fit β values that were at the extreme of the allowed parameter range, as well as a few galaxies with negative SFRs caused by low flux measurements. Average SFR_{UV^{corr}} is in the range 23–320 $M_\odot \text{ yr}^{-1}$ and it increases with redshift. Median SFRs for the individual fits are tabulated for comparison with the mean values. In the highest redshift bin, there is an evident discrepancy between the mean and median values of SFR_{UV^{corr}}.

This discrepancy is caused by a relatively small number of galaxies with extremely high dust corrected SFRs. There are seven galaxies in the highest redshift bin with SFR $> 1000 M_\odot \text{ yr}^{-1}$. Checking the positions of these galaxies against the published LESS catalog (Weiss et al. 2009) indicates that they are not submillimeter sources; separations between these galaxies and their nearest neighbor in the submillimeter catalogue are all greater than $50''$. IRAC colors are available for three of these seven galaxies, and none of them appear in the AGN selection region of Stern et al. (2005) in IRAC color-color space. AGN contamination cannot be ruled out; however, we would expect obscuration of the AGN in restframe UV and optical wavebands to mean that star formation would dominate the emission (as opposed to the case in X-ray wavebands, where obscured AGN are a dominant confounding factor). These outliers may suggest either different dust physical properties or geometry in these galaxies.

In comparison with other literature works, Daddi et al. (2004) determine SFRs for a sample of 24 sBzK galaxies in the GOODS-S field at $z > 1.4$ using SED fitting and dust correction using the method of Meurer et al. (1999), and find dust corrected SFR in the range 100–600 $M_\odot \text{ yr}^{-1}$. In a spectroscopically selected sample of BzKs, Yoshikawa et al. (2010) find SFRs to vary widely, over three orders of magnitude.

We also compute the SFRs from an unweighted average spectrum of galaxies within each redshift bin. The SFRs derived from the average spectra closely match the median SFRs of the individual spectra. The average spec-

trum is apparently less susceptible to outliers in the SFR distribution and appears to be a better representation of a typical sBzK galaxy. By comparing with $\text{SFR}_{\text{IR}+\text{UV}}$, discussed Section 6.1, we conclude that the average SED works better for IRX- β SFR estimation.

The Meurer et al. (1999) correlation between $L_{\text{IR}}/L_{\text{UV}}$ and UV spectral index, β , is commonly used to estimate and correct for dust attenuation, particularly when IR data are unavailable. However, normal star forming galaxies are found to deviate from this relation, having a smaller $L_{\text{IR}}/L_{\text{UV}}$ for a given spectral index, β (e.g. Boissier et al. 2007; Buat et al. 2010), while Ultraluminous Infrared Galaxies (ULIRGs) have been found to have larger than expected $L_{\text{IR}}/L_{\text{UV}}$ from this correlation (e.g. Goldader et al. 2002). Reddy et al. (2006) find that LBGs and BzK galaxies at $1.4 < z < 2.6$ with ages > 100 Myr follow this correlation, while galaxies in this redshift range with ages < 100 Myr show greater dispersion, and tend to have higher β values (i.e. redder colors, greater dust obscuration) for a given IR luminosity.

We measure average $L_{\text{IR}}/L_{\text{UV}}$ independently in our sample of stacked BzKs. Specific UV luminosity values, L_{UV} , in units of $10^{28} \text{ erg s}^{-1} \text{ Hz}^{-1}$ are taken from the unweighted average spectrum in each redshift bin, and converted to luminosity by multiplying by the frequency $\nu = 1.8 \times 10^{15} \text{ Hz}$ (rest frame 1600 \AA), and then converted to units of $10^{11} L_{\odot}$. L_{IR} estimates, obtained from fits of mid-IR through radio photometry ($\lambda \geq 24 \mu\text{m}$) to CE01 templates, are taken from Table 3. The resulting $L_{\text{IR}}/L_{\text{UV}}$ ratios are 14.8, 35.2, 27.8, 18.3 for the redshift bins $0.9 < z \leq 1.2$, $1.2 < z \leq 1.5$, $1.5 < z \leq 2.0$ and $2.0 < z \leq 3.2$ respectively. β values are taken from fits to the unweighted average spectrum in each redshift bin. These data are plotted as $\log(L_{\text{IR}}/L_{\text{UV}})$ vs. β in Figure 6, and are compared to starburst and star forming galaxies at lower redshift ($z < 0.3$) reported in Buat et al. (2010); data for these low redshift systems are indicated as points in Figure 6¹⁶. The $L_{\text{IR}}/L_{\text{UV}} - \beta$ relation for normal star forming galaxies in the local universe reported by Boissier et al. (2007) is indicated by the dashed, cyan curve in the figure. Our redshift binned sBzK estimates match the Meurer et al. (1999) relation, and this agreement gives confidence in the UV corrected SFR estimates. For a given IR luminosity, these systems have on average a bluer UV spectrum than normal star forming galaxies in the local universe, indicative of a younger stellar population and/or diminished dust obscuration compared to local galaxies.

5.3. Radio SFR Estimates

Radio fluxes, luminosities, spectral indices and associated star formation rates are reported in Table 5 and star formation rates are compared to calibrations in other wavebands in Table 7. Upper limits are found in both radio bands in the $0.9 < z \leq 1.2$ redshift bin. The radio spectral indices, determined from 610 MHz and 1.4 GHz data in the $1.2 < z \leq 1.5$ and $2.0 < z \leq 3.2$ red-

shift bins are -0.66 ± 0.34 and -0.84 ± 0.47 , consistent with the value of -0.8 typically observed in star forming galaxies. The radio spectral index in the $1.5 < z \leq 2.0$ bin is unusually steep, -1.37 ± 0.41 , due to the unexpectedly high flux in the 610 MHz band; this high flux estimate is propagated to an unexpectedly high star formation rate in one radio calibration, as discussed below, but otherwise the observations at other wavelengths for this redshift bin are unremarkable.

The radio based SFR estimates from the calibration of Condon (1992) and Bell (2003) are compared in Table 5. It has been reported previously that $\text{SFR}_{1.4\text{GHz}}^{\text{Condon}}$ exceeds $\text{SFR}_{1.4\text{GHz}}^{\text{Bell}}$ by approximately a factor of two (Bell 2003). $\text{SFR}_{1.4\text{GHz}}^{\text{Condon}}$ incorporates separately the effects of synchrotron radiation and thermal free-free emission, whereas $\text{SFR}_{1.4\text{GHz}}^{\text{Bell}}$ is an empirical correlation that uses the IR-Radio correlation. Discrepancies between the radio SFR calibrations of Bell (2003) and Condon (1992) are not entirely surprising given the different assumptions of each calibration.

$\text{SFR}_{1.4\text{GHz}}^{\text{Condon}}$ can be compared to previous reported results for stacking sBzKs; in stacking a $K_{\text{AB}} \leq 23$ sample of BzKs, Dunne et al. (2009) reported a median sBzK luminosity of $1.28 \times 10^{23} \text{ W Hz}^{-1}$ corresponding to $\text{SFR} = 154 \pm 7 \text{ M}_{\odot} \text{ yr}^{-1}$, which is consistent with our $1.2 < z \leq 1.5$ bin result of $139 \pm 32 \text{ M}_{\odot} \text{ yr}^{-1}$, but lower than our higher redshift bin results by a factor of ~ 3 . However, the sample of BzKs reported in Dunne et al. (2009), which is taken from the catalog of Lane et al. (2007), may have been contaminated by low redshift interlopers.

The values of $\text{SFR}_{1.4\text{GHz}}^{\text{Bell}}$ indicated in Table 5 are consistent with UV, and IR based SFR calibrations presented here. The values presented here are closer to but somewhat larger than results from the COSMOS survey; Pannella et al. (2009) reported radio based SFR estimates in the range $30\text{--}100 \text{ M}_{\odot} \text{ yr}^{-1}$ (see their Figure 3; SFR plotted vs B magnitude) for BzKs using the empirical IR-Radio based calibration of Yun et al. (2001).

5.4. X-ray SFR Estimates

Our *Chandra* soft band stacked X-ray fluxes are in the range $8\text{--}19 \times 10^{-18} \text{ erg s}^{-1} \text{ cm}^{-2}$, and hard band stacked X-ray fluxes are in the range $3.4\text{--}9.5 \times 10^{-17} \text{ erg s}^{-1} \text{ cm}^{-2}$, see Table 6. We find fluxes increasing with redshift in both hard and soft bands. Daddi et al. (2005) report a similar soft band ($0.5\text{--}2 \text{ keV}$) flux of $1.0 \times 10^{-17} \text{ erg s}^{-1} \text{ cm}^{-2}$ in stacking sBzKs in GOODS-N and they do not find a stacking detection in the hard band.

Using observed frame, soft band fluxes and our assumed $\Gamma = 1.2$ spectrum to convert flux to luminosity leads to rest frame, 2-10 keV luminosities in the range $1.9\text{--}10.0 \times 10^{41} \text{ erg s}^{-1}$, indicated in Table 6. In comparison with other reported values, Daddi et al. (2004) find rest frame, 2-10 keV luminosity of $8.6 \times 10^{41} \text{ erg s}^{-1}$ in stacking 23 sBzKs in the K20 Survey (Cimatti et al. 2002) that includes part of the CDF-S. Daddi et al. (2005) find a rest frame, 2-10 keV luminosity of $3.4 \times 10^{41} \text{ erg s}^{-1}$ in stacking X-ray undetected sBzKs in 2 Ms *Chandra* data in GOODS-N (they use $\Gamma = 2.0$ in their flux to luminosity conversion). Reddy et al. (2005) report rest frame 2-10 keV luminosities in the

¹⁶ Data from these nearby systems include β values that are estimated from *Galaxy Evolution Explorer* (GALEX) FUV and NUV measurements. We use the empirical calibration of Kong et al. (2004) to transform these β values to be consistent with β estimates obtained from the method of Calzetti et al. (1994) and used in this paper.

range $\approx 3 - 5 \times 10^{41}$ erg s $^{-1}$ in stacking their sample of sBzKs in 2 Ms *Chandra* data in GOODS-N (using $\Gamma = 2.0$ in flux to luminosity conversion; see their Table 1).

Daddi et al. (2007a) report X-ray fluxes for a subsample of sBzKs with strong mid-IR emission that are a factor of ≈ 3.5 greater than other sBzKs (inferred $N_H \sim 10^{24}$ cm $^{-2}$ and unobscured X-ray luminosities, $L_{2-8\text{keV}} \approx 1 - 4 \times 10^{43}$ ergs s $^{-1}$), and they postulate obscured AGN in these sources. Murphy et al. (2009) studied a sample IR-excess BzKs with *Spitzer* IRS spectroscopy and multiwavelength photometry and concluded that a fraction of these IR excess galaxies may have been mis-identified (IR luminosities over-estimated by 24 μ m data), but that the remainder may well harbor obscured AGN.

Our SFRs estimated from the rest frame 2-10 keV luminosities, and the calibration of Ranalli et al. (2003) are in the range 40-200 M $_{\odot}$ yr $^{-1}$, a factor of ≈ 5 lower than the corresponding calibrations of Lehmer et al. (2010) and Persic et al. (2004). As discussed in Section 4.4, $\text{SFR}_{2-10\text{keV}}^{\text{Persic}}$ may be considered to provide upper limits. In the SFR calibration of Lehmer et al. (2010), the stellar mass term contributes <23%, 7%, 3% and 1.4% to the SFRs in each redshift range of Table 7, respectively. The trend of decreasing contribution from LMXBs to the total X-ray luminosity as redshift increases is broadly consistent with models of the LMXB population and star formation history that predict the LMXB population to decline at $z > 1$ (Ghosh & White 2001).

However, interpretation of these X-ray SFRs depends upon an uncertain contamination fraction from obscured AGN. We speculate that AGN contamination may be present in our sample, particularly in the highest redshift bin, in which we find $L_{2-10\text{keV}} \sim 10^{42}$ erg s $^{-1}$. Consequently, X-ray SFRs would be over-estimated. Lehmer et al. (2008) compute a luminosity dependent AGN fraction in order to correct X-ray stacking results in $z \sim 3$ galaxies; they find that $\approx 50 - 70\%$ of the stacked 0.5-2 keV counts may arise from obscured AGN. If a similar AGN fraction exists in our sample, then the X-ray SFRs would need to be adjusted downwards by a factor of 2.5, bringing $\text{SFR}_{2-10\text{keV}}^{\text{Persic}}$ and $\text{SFR}_{2-10\text{keV}}^{\text{Lehmer}}$ into better agreement with other waveband indicators, as discussed in Section 6.1, and taking $\text{SFR}_{2-10\text{keV}}^{\text{Ranalli}}$ out of agreement with these other waveband indicators.

6. DISCUSSION

6.1. Comparison of SFR Estimates

SFR estimates from X-ray through radio calibrations are compared in Table 7. The SFR_{IR} values in Table 7 are obtained from L_{IR} estimates from fits of MIR-radio ($\lambda \geq 24\mu\text{m}$) photometry to CE01 templates. To gauge their consistency, we plot the ratio of SFR computed from each calibration to $\text{SFR}_{\text{IR}+\text{UV}}$ in Figure 7. In this figure, $\text{SFR}_{\text{IR}}/\text{SFR}_{\text{IR}+\text{UV}}$ is most nearly equal to one, reflecting that IR luminosity accounts for >90% of the total SFR in these galaxies. This fraction will be substantially less in galaxies with significantly lower dust amounts, such as Ly α -Emitting Galaxies (e.g. Gawiser et al. 2007; Guaita et al. 2010).

Comparing $\text{SFR}_{24\mu\text{m}}$ to $\text{SFR}_{\text{IR}+\text{UV}}$ in Table 7 and Figure 7 illustrates the overestimate of SFR at high redshift from this single waveband estimate. The resulting poor

fit to the data in the highest redshift bin, $2.0 < z \leq 3.2$, illustrated in Figure 4, overestimates L_{IR} by approximately a factor of 6. Although 24 μ m estimates of L_{IR} can be robust at $z < 1.5$ (e.g. Elbaz et al. 2010), overestimation of L_{IR} , particularly at higher redshift has been previously reported (e.g. Papovich et al. 2007; Murphy et al. 2009; Muzzin et al. 2010; Nordon et al. 2010). We conclude that 24 μ m only based SFR estimates should be interpreted with great caution and avoided at $z > 2$.

We find dust corrected UV SFR from individual fits to sBzK photometry to agree with $\text{SFR}_{\text{IR}+\text{UV}}$ at each redshift, although the highest redshift bin exhibits larger $\text{SFR}_{\text{UV}}^{\text{Corr}}$ and also larger error than lower redshift bins. As discussed in Section 5.2, this large SFR value is strongly affected by a small number of outliers. Notably, $\text{SFR}_{\text{UV}}^{\text{Corr}}$ values determined from the average spectrum, shown in Table 4, are in excellent agreement with $\text{SFR}_{\text{IR}+\text{UV}}$ at all redshifts. In addition to being conceptually similar to the stacking analysis used at other wavelengths, using the average spectrum to determine the UV SFR appears to be more robust against outliers than analysis of individual galaxies.

Agreement between dust corrected UV SFR and $\text{SFR}_{\text{IR}+\text{UV}}$ in BzKs, typically to within a factor of ~ 2 has been reported previously (e.g. Reddy et al. 2006; Daddi et al. 2007b; Nordon et al. 2010). Reddy et al. (2010) find $\text{SFR}_{\text{UV}}^{\text{Corr}}$ to agree with SFR determined from H α spectroscopy for LBGs at $z \sim 2$. In particular, Reddy et al. (2006) find LBGs and BzKs with ages > 100 Myr to follow the Meurer et al. (1999) relation while LBGs and BzKs with ages < 100 Myr have rest UV colors that are redder than expected for a given $L_{\text{IR}+\text{UV}}$. In comparing $\text{SFR}_{\text{UV}}^{\text{Corr}}$ with $\text{SFR}_{\text{IR}+\text{UV}}$, we find the best agreement in the lower redshift bins, and we find $\text{SFR}_{\text{UV}}^{\text{Corr}}$ to be an overestimate in the highest redshift bin. These lines of evidence are consistent with a modified extinction law for at least some galaxies above $z \sim 2$.

Among radio based SFR estimates, Figure 7 illustrates agreement between $\text{SFR}_{1.4\text{GHz}}^{\text{Bell}}$ and $\text{SFR}_{\text{IR}+\text{UV}}$ to within a factor of two over our redshift range; however, this agreement is a consequence of the IR-Radio correlation for sBzKs, and is not indicative of a truly independent estimate of star formation. The model of Condon (1992) does estimate star formation from radio luminosity independent of the IR-Radio correlation; $\text{SFR}_{1.4\text{GHz}}^{\text{Condon}}$ exceeds $\text{SFR}_{\text{IR}+\text{UV}}$ by a factor of 2-4 over the observed redshift range, but the ratio of these two calibrations appears relatively insensitive to redshift. The discrepancies between the radio SFR calibrations of Bell (2003) and Condon (1992) are not entirely surprising given the different assumptions of each calibration.

X-ray SFR indicators show wide variation in their ratios to $\text{SFR}_{\text{IR}+\text{UV}}$. As discussed in Section 5.4, $\text{SFR}_{2-10\text{keV}}^{\text{Persic}}$ may be interpreted as an upper limit. $\text{SFR}_{2-10\text{keV}}^{\text{Lehmer}}$ yields estimates that are similar to $\text{SFR}_{2-10\text{keV}}^{\text{Persic}}$ because of the subdominant contribution of the stellar mass term to the X-ray luminosity in these galaxies. Meanwhile $\text{SFR}_{2-10\text{keV}}^{\text{Ranalli}}$, actually agrees with $\text{SFR}_{\text{IR}+\text{UV}}$ to within a factor of two. $\text{SFR}_{2-10\text{keV}}^{\text{Ranalli}}$ has been applied to BzKs (e.g. Daddi et al. 2007a; Reddy et al. 2005), BX/BM galaxies (e.g. Reddy & Yun 2004), and LBGs at $z \sim 2$ (e.g. Reddy et al. 2010). In these

studies, X-ray SFRs often agree with other waveband estimators, typically to within the same factors as reported here. Given the discussion in Section 4.4 about the different components to X-ray luminosity and their relation to star formation, this agreement is probably misleading. AGN contamination even at the level of 10% can require downward adjustment to X-ray SFRs by a factor of 2-5 (Lehmer et al. 2008). Such correction would bring $\text{SFR}_{2-10\text{keV}}^{\text{Persic}}$ and $\text{SFR}_{2-10\text{keV}}^{\text{Lehmer}}$ into better agreement with other wavebands, and $\text{SFR}_{2-10\text{keV}}^{\text{Ranalli}}$ would then be an underestimate of the true SFR.

In computing uncertainties in these SFR estimates, we have considered the effects of errors in photometry, spectral shape and redshift on luminosity estimates. We have excluded the uncertainty due to luminosity – SFR calibration. We are not able to assess the absolute uncertainties in these SFR calibrations because in many cases they contain implicit dependencies on L_{IR} –SFR calibration. SFR_{IR} , $\text{SFR}_{24\mu\text{m}}$, $\text{SFR}_{1.4\text{GHz}}^{\text{Bell}}$, $\text{SFR}_{2-10\text{keV}}^{\text{Ranalli}}$ and $\text{SFR}_{2-10\text{keV}}^{\text{Persic}}$ depend implicitly upon the L_{IR} –SFR calibration of Kennicutt (1998b), which has a reported systematic uncertainty of about a factor of 2-3. Similarly, $\text{SFR}_{2-10\text{keV}}^{\text{Lehmer}}$ depends upon the L_{IR} –SFR calibration of Bell et al. (2005), which also has a reported systematic uncertainty of a factor of 2. Similarly, $\text{SFR}_{\text{UV}}^{\text{Corr}}$ depends upon a model dependent UV luminosity – SFR calibration, for which various published values may differ by a factor of 2 (Kennicutt 1998a). In the comparisons discussed here, we assume that the various SFR calibrations are consistent with each other and do not evolve with redshift. We compare them against each other, and disagreement can provide evidence of systematic offsets in a given calibration. A more complete assessment of systematic uncertainties in these SFR calibrations is beyond the scope of this paper.

6.2. sBzK Contribution to Star Formation Rate Density

Ascertaining the cosmic star formation rate density, SFRD, at all redshifts will pose important constraints on galaxy evolution theory. However, current photometric selection methods are invariably incomplete, and therefore cosmic SFRD cannot be measured by studying sBzK galaxies alone. Nevertheless, in order to compare our results with the literature, and to determine the contribution of this color selected sample to the total SFRD, we have determined the SFRD for sBzKs in each redshift bin, using the volume densities of our sample indicated in Table 1 and the star formation rates indicated in Table 7. Multiplying the values of $\text{SFR}_{\text{IR}+\text{UV}}$ indicated in Table 7 by the corresponding comoving volume densities indicated in Table 1, we obtain values of the sBzK contribution to the SFRD of $8 \pm 2 \times 10^{-4}$, 0.010 ± 0.001 , 0.014 ± 0.002 , $0.005 \pm 0.001 \text{ M}_{\odot} \text{ yr}^{-1} \text{ Mpc}^{-3}$ for the redshift bins $0.9 < z \leq 1.2$, $1.2 < z \leq 1.5$, $1.5 < z \leq 2.0$, $2.0 < z \leq 3.2$ respectively. These values are illustrated in Figure 8.

Yoshikawa et al. (2010) measured the sBzK contribution to the SFRD to be between $0.029^{+0.002}_{-0.002}$ and $0.136^{+0.020}_{-0.028} \text{ M}_{\odot} \text{ yr}^{-1} \text{ Mpc}^{-3}$ (depending upon assumptions for dust extinction) in a sample of $K_{\text{SAB}} < 23$ selected sBzKs in the range $1.5 \lesssim z \lesssim 2.5$ that were studied with H α spectroscopy. In order to make a com-

parison with this deeper sample, we attempt to correct for the shallower K band imaging depth of the present survey, which has a $K_{\text{Vega}} < 20$ ($K_{\text{AB}} < 21.8$), and estimate the number of sBzKs that are missed. McCracken et al. (2010) report sBzK number counts to a depth of $K_{\text{SAB}} < 23$. In estimating the number of missed sBzKs in our K band image, we assume the same fraction of AGN and poor redshift estimates as the present survey (18%). With these assumptions, the deeper imaging of McCracken et al. (2010) predicts 5000 additional sources in the ECDF-S that are not detected in the shallower MUSYC K -band image. Assuming these additional sources have the same redshift distribution as the detected sample, then these undetected sBzKs would contribute an additional volume density of $6.18 \times 10^{-4} \text{ Mpc}^{-3}$, $1.69 \times 10^{-3} \text{ Mpc}^{-3}$, $1.29 \times 10^{-3} \text{ Mpc}^{-3}$, $3.33 \times 10^{-4} \text{ Mpc}^{-3}$ respectively to the redshift binned volume densities indicated in Table 1. The corresponding increased SFRDs for each redshift bin are computed, using the $\text{SFR}_{\text{IR}+\text{UV}}$ estimates in Table 7. They are indicated as red triangles in Figure 8; given the uncertainties, these corrected sBzK contributions to SFRD are consistent with the results of Yoshikawa et al. (2010). This figure also illustrates the cosmic star formation history from other investigations, as compiled in Hopkins (2007).

Figure 8 illustrates that the contribution of sBzKs to the total cosmic star formation peaks in the redshift range $1.5 < z \leq 2.0$, which is consistent with BzK selection being most efficient in this range. In this redshift range, averaged sBzKs contribute ~ 20 -50% to the total cosmic star formation rate density. However, sBzKs are the broadest color classification of high redshift, star forming galaxies; e.g. they encompass as much as 80% of BM/BX/LBG galaxies when these latter sources are detected to a comparable K band limit (Reddy et al. 2005). Together, these findings may suggest that the distribution of star formation rates in these galaxies is skewed such that relatively rare, high star formation rate systems contribute disproportionately to the total cosmic SFRD, as is found with submillimeter galaxies (Blain et al. 2002). However the combination of a flux-limited survey with color selection efficiencies being a function of redshift makes it very difficult to infer evolution from these average SFRs.

7. CONCLUSION

The main results of this paper are summarized in Table 7 and Figure 7. For sBzKs in the redshift range $0.9 < z \leq 3.2$, we find SFR_{IR} contributes $> 90\%$ of the total SFR, here defined as $\text{SFR}_{\text{IR}+\text{UV}} \equiv \text{SFR}_{\text{IR}} + \text{SFR}_{\text{UV}}$. In the highest redshift bin, $2.0 < z \leq 3.2$, IR luminosities and SFR estimates from $24 \mu\text{m}$ only data fit to fixed luminosity CE01 templates exceed IR luminosity from panchromatic SED fitting and total SFR by a factor of ≈ 6 . Fitting panchromatic SEDs to spectral templates yields a more robust estimate of the IR luminosity than single band estimates. In particular, the $24 \mu\text{m}$ band only estimate should be avoided for galaxies at $z \gtrsim 2$.

Dust corrected UV SFR, using the method of Meurer et al. (1999), agrees to within errors with $\text{SFR}_{\text{IR}+\text{UV}}$. Independent L_{IR} estimates demonstrate that sBzKs follow the Meurer et al. (1999) relation of $L_{\text{IR}}/L_{\text{UV}}$ vs. β for starburst galaxies as opposed to the correspond-

ing relation for normal star forming galaxies in the local universe or AGN. We find dust corrected UV SFRs obtained from the average SED to be in better agreement with SFR_{IR+UV} than the average of individual dust corrected SFRs, and therefore we recommend this approach.

Radio SFRs estimated from the calibration of Bell (2003) are in agreement with total SFRs to within errors. The calibration of Bell (2003) is an indirect estimate of IR luminosity using the far IR-radio correlation, as opposed to an independent calibration based on radio luminosity alone. The SFR calibration of Condon (1992) uses an independent model of radio emission and overestimates total SFR by factors of 2-4 over this redshift range.

Our X-ray SFR calibrations are difficult to interpret in the light of potential AGN contamination, particularly in the highest redshift bin. Perhaps surprisingly, the calibration of Ranalli et al. (2003) yields SFR estimates that agree with SFR_{IR+UV} and other indicators, while the better suited X-ray calibrations of Persic et al. (2004) and Lehmer et al. (2010) over-estimate SFR. This circumstance is probably a coincidence caused by mild AGN contamination, which would bring $\text{SFR}_{2-10\text{keV}}^{\text{Persic}}$ and $\text{SFR}_{2-10\text{keV}}^{\text{Lehmer}}$ into rough agreement with SFR_{IR+UV} and cause $\text{SFR}_{2-10\text{keV}}^{\text{Ranalli}}$ to underestimate SFR.

Our analysis of $K_{AB} < 21.8$ sBzKs in the redshift range $0.9 < z \leq 3.2$ confirms that they are IR luminous, star forming galaxies for which approximately 90% of the total star formation is obscured by dust. By fitting to CE01 templates, we find average IR luminosities for redshift binned sBzK galaxies at median redshifts 1.1, 1.4, 1.8, 2.2 to be $0.6 \pm 0.2 \times 10^{11} L_{\odot}$, $3.2 \pm 0.4 \times 10^{11} L_{\odot}$, $5.5 \pm 0.8 \times 10^{11} L_{\odot}$, $6.9 \pm 1.6 \times 10^{11} L_{\odot}$, consistent with the luminosities of LIRGs in the local universe. By fitting the redshift bin averaged spectra in the range $1.2 < z \leq 1.5$ and $1.5 < z \leq 2.0$ to gray body templates, we find average dust temperatures of 41 K and 43 K respectively, consistent with star formation induced heating. We find SFR_{IR+UV} at these redshifts to be 12 ± 2.8 , 58 ± 7.0 , 100 ± 14 , $130 \pm 28 M_{\odot} \text{ yr}^{-1}$ respectively, and we obtain values of the sBzK contribution to the SFRD to be $8 \pm 2 \times 10^{-4}$, 0.010 ± 0.001 , 0.014 ± 0.002 , $0.005 \pm 0.001 M_{\odot} \text{ yr}^{-1} \text{ Mpc}^{-3}$. These contributions to the SFRD are affected by the relatively shallow K band imaging depth of our data, compared to other surveys. Based on extrapolating the galaxy number counts to the faintest reported imaging depth for sBzKs, we estimate their contribution to the cosmic SFRD to be $\sim 20\%$ in the redshift range $1.5 < z \leq 2.0$ where sBzK selection is most efficient.

We acknowledge valuable conversations and comments by Viviana Acquaviva, Eric Bell, Nicholas Bond, Lucia Guaita, Bret Lehmer, Felipe Menanteau, and Axel Weiss and we thank LESS for providing the 870 μm data, obtained from LABOCA APEX RUN IDs: 078.F-9028(A), 079.F-9500(A), 080.A-3023(A), and 081.F-9500(A). Support for this work was provided by the National Science Foundation under grant AST-0807570, and by NASA through an award issued by JPL/Caltech. EG thanks U.C. Davis for hospitality during the preparation of this manuscript. Support for the work of ET was provided by the National Aeronautics and Space Administration through Chandra Postdoctoral Fellowship Award Num-

ber PF8-90055 issued by the Chandra X-ray Observatory Center, which is operated by the Smithsonian Astrophysical Observatory for an on behalf of the National Aeronautics and Space Administration under contract NAS8-03060.

8. APPENDIX: ERROR ESTIMATION IN STACKING

8.1. Ordinary Average

Section 3 presents the method used in this paper for estimating the aggregate flux, μ , from N prior positions that include a combination of I individual detections, x_i , and a stacking detection, x_s , from S undetected sources, where $N = I + S$, given by

$$\mu = \frac{1}{N} \left(\sum_{i=1}^I x_i + S x_s \right) \quad (16)$$

The variance σ_{μ}^2 of this estimate is related to the individual errors σ_i and σ_s as well as their covariances, $\sigma_{i,s}$ from standard error analysis

$$\sigma_{\mu}^2 = \sum_{i=1}^I \left(\frac{\partial \mu}{\partial x_i} \right)^2 \sigma_{x_i}^2 + \left(\frac{\partial \mu}{\partial x_s} \right)^2 \sigma_{x_s}^2 + \sum_{i=1}^I 2 \sigma_{i,s}^2 \frac{\partial \mu}{\partial x_i} \frac{\partial \mu}{\partial x_s} + \dots \quad (17)$$

We assume that the covariances $\sigma_{i,s}$ are zero.

$$\sigma_{\mu}^2 = \sum_{i=1}^I \left(\frac{\partial \mu}{\partial x_i} \right)^2 \sigma_{x_i}^2 + \left(\frac{\partial \mu}{\partial x_s} \right)^2 \sigma_{x_s}^2 \quad (18)$$

$$\sigma_{\mu}^2 = \frac{1}{N^2} \sum_{i=1}^I \sigma_{x_i}^2 + \left(\frac{S}{N} \right)^2 \sigma_{x_s}^2 \quad (19)$$

$$\sigma_{\mu} = \frac{1}{N} \sqrt{\sum_{i=1}^I \sigma_{x_i}^2 + S^2 \sigma_{x_s}^2} \quad (20)$$

Equations 16 and 20 are used to compute the average and error, respectively, of individual and stacking detections reported in this paper.

In the case of all measurement errors being equal, which is a good approximation in the case of LESS data, then $\sigma_i \equiv \sigma$ and $\sigma_s = \sigma/\sqrt{N}$. Using Equation 20, σ_{μ} is computed as

$$\sigma_{\mu} = \frac{1}{N} \sqrt{\sum_{i=1}^I \sigma^2 + S^2 \frac{\sigma^2}{S}} \quad (21)$$

$$\sigma_{\mu} = \frac{1}{I+S} \sqrt{I\sigma^2 + S\sigma^2} \quad (22)$$

$$\sigma_{\mu} = \frac{1}{\sqrt{I+S}} \sigma \quad (23)$$

8.2. Weighted average:

An alternative approach to combining individual and stacking detections into a single aggregate flux estimate is to use a weighted average of individual and stacking detections. Assume there are $N = I + 1$ flux measurements consisting of I individual detections and a single stacking detection. Each individual flux measurement

and the stacked flux measurement is considered as an independent flux measurement for the purpose of computing an average, and these measurements are combined as an inverse variance weighted average.

$$\mu' = \frac{\sum_{i=1}^N \frac{x_i}{\sigma_i^2}}{\sum_{i=1}^N \frac{1}{\sigma_i^2}} \quad (24)$$

$$\sigma_{\mu'}^2 = \frac{1}{\sum_{i=1}^N \frac{1}{\sigma_i^2}} \quad (25)$$

Equations 24 and 25 are also used to estimate the aggregate flux and error for representative data reported in this paper. In particular, the errors computed according to this method are numerically equal to the errors computed from the ordinary average, Equation 20, to better than three significant digits.

For clarity, Equation 25 can be written to include stacking and individual detections separately

$$\sigma_{\mu'}^2 = \frac{1}{\sum_{i=1}^I \frac{1}{\sigma_i^2} + \frac{1}{\sigma_s^2}} \quad (26)$$

In the case of all measurement errors being equal, Equation 26 can be simplified using $\sigma_i \equiv \sigma$ and $\sigma_s = \sigma/\sqrt{N}$, just as in the ordinary average error computation:

$$\sigma_{\mu'}^2 = \frac{1}{\sum_{i=1}^I \frac{1}{\sigma^2} + \frac{S}{\sigma^2}} \quad (27)$$

$$\sigma_{\mu'}^2 = \frac{\sigma^2}{I + S} \quad (28)$$

$$\sigma_{\mu'} = \frac{\sigma}{\sqrt{I + S}} \quad (29)$$

Thus for the case of all measurement errors being equal, the error of the weighted average is identical to the error of the ordinary average.

8.3. Comparison of ordinary and weighted average:

In the case of identical errors for the individual measurements, $\sigma_i \equiv \sigma$, then weighted and ordinary averages give the same result for the aggregate flux. In the case of measurement errors being unequal, then the weighted average will in principle have the smaller error; however, the difference will be small, and if the errors are not independent, e.g. if brighter sources have larger errors, then the weighted average introduces a bias to the flux estimate μ' . For instance, if dim sources are always measured with better precision than bright sources, then a weighted average of the population of all sources will always be biased toward dim sources. This circumstance could arise if flux measurement errors are dominated by Poisson counting statistics. However, if the flux measurement errors are uncorrelated with the flux, then there will be no problem with the weighted average.

REFERENCES

- Adelberger, K. L. & Steidel, C. C. 2000, *ApJ*, 544, 218
 Bauer, F. E., Alexander, D. M., Brandt, W. N., Hornschemeier, A. E., Vignali, C., Garmire, G. P., & Schneider, D. P. 2002, *AJ*, 124, 2351
 Bell, E. F. 2003, *ApJ*, 586, 794
 Bell, E. F., Papovich, C., Wolf, C., Le Floch, E., Caldwell, J. A. R., Barden, M., Egami, E., et al. 2005, *ApJ*, 625, 23
 Blain, A. W., Smail, I., Ivison, R. J., Kneib, J., & Frayer, D. T. 2002, *Phys. Rep.*, 369, 111
 Blanc, G. A., Lira, P., Barrientos, L. F., Aguirre, P., Francke, H., Taylor, E. N., et al. 2008, *ApJ*, 681, 1099
 Boissier, S., Gil de Paz, A., Boselli, A., Madore, B. F., Buat, V., Cortese, L., Burgarella, D., et al. 2007, *ApJS*, 173, 524
 Brammer, G. B., van Dokkum, P. G., & Coppi, P. 2008, *ApJ*, 686, 1503
 Brandt, W. N. & Hasinger, G. 2005, *ARA&A*, 43, 827
 Buat, V., Giovannoli, E., Burgarella, D., Altieri, B., Amblard, A., Arumugam, V., Aussel, H., et al. 2010, *ArXiv e-prints*
 Calzetti, D. 2008, in *Astronomical Society of the Pacific Conference Series*, Vol. 390, *Pathways Through an Eclectic Universe*, ed. J. H. Knapen, T. J. Mahoney, & A. Vazdekis, 121+
 Calzetti, D., Kinney, A. L., & Storchi-Bergmann, T. 1994, *ApJ*, 429, 582
 Cardamone, C. N., van Dokkum, P. G., Urry, C. M., Taniguchi, Y., Gawiser, E., Brammer, G., Taylor, E., et al. 2010, *ApJS*, 189, 270
 Chary, R. & Elbaz, D. 2001, *ApJ*, 556, 562
 Cimatti, A., Daddi, E., Mignoli, M., Pozzetti, L., Renzini, A., Zamorani, G., Broadhurst, T., et al. 2002, *A&A*, 381, L68
 Colbert, E. J. M., Heckman, T. M., Ptak, A. F., Strickland, D. K., & Weaver, K. A. 2004, *ApJ*, 602, 231
 Condon, J. J. 1974, *ApJ*, 188, 279
 —. 1992, *ARA&A*, 30, 575
 Daddi, E., Alexander, D. M., Dickinson, M., Gilli, R., Renzini, A., Elbaz, D., Cimatti, A., et al. 2007a, *ApJ*, 670, 173
 Daddi, E., Cimatti, A., Renzini, A., Fontana, A., Mignoli, M., Pozzetti, L., Tozzi, P., & Zamorani, G. 2004, *ApJ*, 617, 746
 Daddi, E., Dickinson, M., Chary, R., Pope, A., Morrison, G., Alexander, D. M., Bauer, F. E., et al. 2005, *ApJ*, 631, L13
 Daddi, E., Dickinson, M., Morrison, G., Chary, R., Cimatti, A., Elbaz, D., Frayer, D., et al. 2007b, *ApJ*, 670, 156
 Damen, M., Labbe, I., van Dokkum, P., Franx, M., Taylor, E., Brandt, W., Dickinson, M., et al. 2010, *ApJ*, in press
 Dannerbauer, H., Daddi, E., Onodera, M., Kong, X., Röttgering, H., Arimoto, N., et al. 2006, *ApJ*, 637, L5
 Devlin, M. J., Ade, P. A. R., Aretxaga, I., Bock, J. J., Chapin, E. L., Griffin, M., Gundersen, J. O., et al. 2009, *Nature*, 458, 737
 Dunne, L., Ivison, R. J., Maddox, S., Cirasuolo, M., Mortier, A. M., Foucaud, S., Ibar, E., et al. 2009, *MNRAS*, 394, 3
 Elbaz, D., Hwang, H. S., Magnelli, B., Daddi, E., Aussel, H., Altieri, B., Amblard, A., et al. 2010, *A&A*, 518, L29+
 Fabbiano, G. 2006, *ARA&A*, 44, 323
 Gawiser, E., Francke, H., Lai, K., Schawinski, K., Gronwall, C., Ciardullo, R., Quadri, R., et al. 2007, *ApJ*, 671, 278
 Gawiser, E., van Dokkum, P. G., Herrera, D., Maza, J., Castander, F. J., Infante, L., Lira, P., et al. 2006, *ApJS*, 162, 1
 Ghosh, P. & White, N. E. 2001, *ApJ*, 559, L97
 Goldader, J. D., Meurer, G., Heckman, T. M., Seibert, M., Sanders, D. B., Calzetti, D., & Steidel, C. C. 2002, *ApJ*, 568, 651
 Greve, T. R., Weiß, A., Walter, F., Smail, I., Zheng, X. Z., Knudsen, K. K., Coppin, K. E. K., et al. 2010, *ApJ*, 719, 483
 Grimm, H., Gilfanov, M., & Sunyaev, R. 2003, *MNRAS*, 339, 793
 Guaita, L., Gawiser, E., Padilla, N., Francke, H., Bond, N. A., Gronwall, C., Ciardullo, R., et al. 2010, *ApJ*, 714, 255
 Haarsma, D. B., Partridge, R. B., Windhorst, R. A., & Richards, E. A. 2000, *ApJ*, 544, 641
 Hayashi, M., Shimasaku, K., Motohara, K., Yoshida, M., Okamura, S., & Kashikawa, N. 2007, *ApJ*, 660, 72
 Hogg, D. W. 2001, *AJ*, 121, 1207
 Hopkins, A. M. 2007, in *Astronomical Society of the Pacific Conference Series*, Vol. 380, *Deepest Astronomical Surveys*, ed. J. Afonso, H. C. Ferguson, B. Mobasher, & R. Norris, 423+
 Howell, J. H., Armus, L., Mazzarella, J. M., Evans, A. S., Surace, J. A., Sanders, D. B., Petric, A., et al. 2010, *ApJ*, 715, 572

- Huynh, M. T., Pope, A., Frayer, D. T., & Scott, D. 2007, *ApJ*, 659, 305
- Iverson, R. J., Alexander, D. M., Biggs, A. D., Brandt, W. N., Chapin, E. L., Coppin, K. E. K., Devlin, M. J., et al. 2010a, *MNRAS*, 402, 245
- Iverson, R. J., Chapman, S. C., Faber, S. M., Smail, I., Biggs, A. D., Conselice, C. J., Wilson, G., et al. 2007, *ApJ*, 660, L77
- Iverson, R. J., Magnelli, B., Ibar, E., Andreani, P., Elbaz, D., Altieri, B., Amblard, A., et al. 2010b, *A&A*, 518, L31+
- Kannappan, S. J. & Gawiser, E. 2007, *ApJ*, 657, L5
- Kennicutt, R. C., Hao, C., Calzetti, D., Moustakas, J., Dale, D. A., Bendo, G., Engelbracht, C. W., Johnson, B. D., & Lee, J. C. 2009, *ApJ*, 703, 1672
- Kennicutt, Jr., R. C. 1998a, *ARA&A*, 36, 189
- . 1998b, *ApJ*, 498, 541
- Kong, X., Charlot, S., Brinchmann, J., & Fall, S. M. 2004, *MNRAS*, 349, 769
- Kong, X., Daddi, E., Arimoto, N., Renzini, A., Broadhurst, T., Cimatti, A., Ikuta, C., et al. 2006, *ApJ*, 638, 72
- Kroupa, P. 2001, in *Astronomical Society of the Pacific Conference Series*, Vol. 228, *Dynamics of Star Clusters and the Milky Way*, ed. S. Deiters, B. Fuchs, A. Just, R. Spurzem, & R. Wielen, 187–+
- Kurczynski, P. & Gawiser, E. 2010, *AJ*, 139, 1592
- Lane, K. P., Almaini, O., Foucaud, S., Simpson, C., Smail, I., McLure, R. J., Conselice, C. J., et al. 2007, *MNRAS*, 379, L25
- Lehmer, B. D. 2010, private communication
- Lehmer, B. D., Alexander, D. M., Bauer, F. E., Brandt, W. N., Goulding, A. D., Jenkins, L. P., Ptak, A., & Roberts, T. P. 2010, *ApJ*, 724, 559
- Lehmer, B. D., Brandt, W. N., Alexander, D. M., Bauer, F. E., Schneider, D. P., Tozzi, P., Bergeron, J., et al. 2005, *ApJS*, 161, 21
- Lehmer, B. D., Brandt, W. N., Alexander, D. M., Bell, E. F., Hornschemeier, A. E., McIntosh, D. H., Bauer, F. E., et al. 2008, *ApJ*, 681, 1163
- Leitherer, C. & Heckman, T. M. 1995, *ApJS*, 96, 9
- Lutovinov, A., Revnivtsev, M., Gilfanov, M., Shtykovskiy, P., Molkov, S., & Sunyaev, R. 2005, *A&A*, 444, 821
- Madau, P. 1995, *ApJ*, 441, 18
- Madau, P., Pozzetti, L., & Dickinson, M. 1998, *ApJ*, 498, 106
- Marsden, G., Ade, P. A. R., Bock, J. J., Chapin, E. L., Devlin, M. J., Dicker, S. R., Griffin, M., et al. 2009, *ApJ*, 707, 1729
- McCracken, H. J., Capak, P., Salvato, M., Aussel, H., Thompson, D., Daddi, E., Sanders, D. B., et al. 2010, *ApJ*, 708, 202
- Meurer, G. R., Heckman, T. M., & Calzetti, D. 1999, *ApJ*, 521, 64
- Miller, N. A., Fomalont, E. B., Kellermann, K. I., Mainieri, V., Norman, C., Padovani, P., Rosati, P., & Tozzi, P. 2008, *ApJS*, 179, 114
- Murphy, E. J., Chary, R., Alexander, D. M., Dickinson, M., Magnelli, B., Morrison, G., Pope, A., & Teplitz, H. I. 2009, *ApJ*, 698, 1380
- Muzzin, A., van Dokkum, P., Kriek, M., Labbé, I., Cury, I., Marchesini, D., & Franx, M. 2010, *ApJ*, 725, 742
- Nandra, K., Mushotzky, R. F., Arnaud, K., Steidel, C. C., Adelberger, K. L., Gardner, J. P., Teplitz, H. I., & Windhorst, R. A. 2002, *ApJ*, 576, 625
- Nordon, R., Lutz, D., Shao, L., Magnelli, B., Berta, S., Altieri, B., Andreani, P., et al. 2010, *A&A*, 518, L24+
- Overzier, R. A., Heckman, T. M., Wang, J., Armus, L., Buat, V., Howell, J., Meurer, G., et al. 2011, *The Astrophysical Journal Letters*, 726, L7
- Pannella, M., Carilli, C. L., Daddi, E., McCracken, H. J., Owen, F. N., Renzini, A., Strazzullo, V., et al. 2009, *ApJ*, 698, L116
- Papovich, C., Rudnick, G., Le Floc'h, E., van Dokkum, P. G., Rieke, G. H., Taylor, E. N., Armus, L., et al. 2007, *ApJ*, 668, 45
- Peeters, E., Spoon, H. W. W., & Tielens, A. G. G. M. 2004, *ApJ*, 613, 986
- Persic, M. & Rephaeli, Y. 2002, *A&A*, 382, 843
- . 2007, *A&A*, 463, 481
- Persic, M., Rephaeli, Y., Braito, V., Cappi, M., Della Ceca, R., Franceschini, A., & Gruber, D. E. 2004, *A&A*, 419, 849
- Ranalli, P., Comastri, A., & Setti, G. 2003, *A&A*, 399, 39
- Reddy, N. A., Erb, D. K., Pettini, M., Steidel, C. C., & Shapley, A. E. 2010, *ApJ*, 712, 1070
- Reddy, N. A., Erb, D. K., Steidel, C. C., Shapley, A. E., Adelberger, K. L., & Pettini, M. 2005, *ApJ*, 633, 748
- Reddy, N. A., Steidel, C. C., Fadda, D., Yan, L., Pettini, M., Shapley, A. E., Erb, D. K., & Adelberger, K. L. 2006, *ApJ*, 644, 792
- Reddy, N. A. & Yun, M. S. 2004, *ApJ*, 600, 695
- Salpeter, E. E. 1955, *ApJ*, 121, 161
- Sargent, M. T., Schinnerer, E., Murphy, E., Carilli, C. L., Helou, G., Aussel, H., Le Floc'h, E., et al. 2010, *ApJ*, 714, L190
- Silva, L., Granato, G. L., Bressan, A., & Danese, L. 1998, *ApJ*, 509, 103
- Stern, D., Eisenhardt, P., Gorjian, V., Kochanek, C. S., Caldwell, N., Eisenstein, D., Brodwin, M., et al. 2005, *ApJ*, 631, 163
- Symeonidis, M., Willner, S. P., Rigopoulou, D., Huang, J., Fazio, G. G., & Jarvis, M. J. 2008, *MNRAS*, 385, 1015
- Takagi, T., Ono, Y., Shimasaku, K., & Hanami, H. 2008, *MNRAS*, 389, 775
- Takeuchi, T. T., Buat, V., Heinis, S., Giovannoli, E., Yuan, F., Iglesias-Páramo, J., Murata, K. L., & Burgarella, D. 2010, *A&A*, 514, A4+
- Taylor, E. N., Franx, M., van Dokkum, P. G., Quadri, R. F., Gawiser, E., Bell, E. F., Barrientos, L. F., et al. 2009, *ApJS*, 183, 295
- Tielens, A. G. G. M. 2008, *ARA&A*, 46, 289
- Truch, M. D. P., Ade, P. A. R., Bock, J. J., Chapin, E. L., Devlin, M. J., Dicker, S., Griffin, M., et al. 2008, *ApJ*, 681, 415
- Virani, S. N., Treister, E., Urry, C. M., & Gawiser, E. 2006, *AJ*, 131, 2373
- Weiss, A., Kovacs, A., Coppin, K., Greve, T. R., Walter, F., Smail, I., Dunlop, J. S., et al. 2009, *ApJ*, 707
- Yoshikawa, T., Akiyama, M., Kajisawa, M., Alexander, D. M., Ohta, K., Suzuki, R., Tokoku, C., et al. 2010, *ApJ*, 718, 112
- Yun, M. S., Reddy, N. A., & Condon, J. J. 2001, *ApJ*, 554, 803

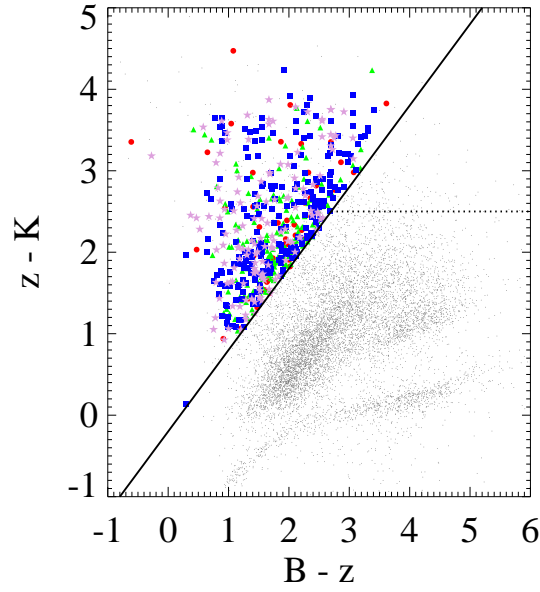


FIG. 1.— BzK diagram illustrating corrected NIR-optical colors $(z - K)_{AB}$ vs. $(B - z)_{AB}$ for MUSYC $K < 21.8$ selected sources (gray points), including redshift binned, star forming galaxies (with X-ray detected AGN removed, see text) in the range $0.9 < z \leq 1.2$ (red circles), $1.2 < z \leq 1.5$ (green triangles), $1.5 < z \leq 2.0$ (blue squares) and $2.0 < z \leq 3.2$ (purple stars). The *sBzK* region is located above the diagonal line, and is defined as $BzK \geq 0.2$. The *pBzK* region is the wedge shaped area defined by the horizontal dotted line, $z - K = 2.5$.

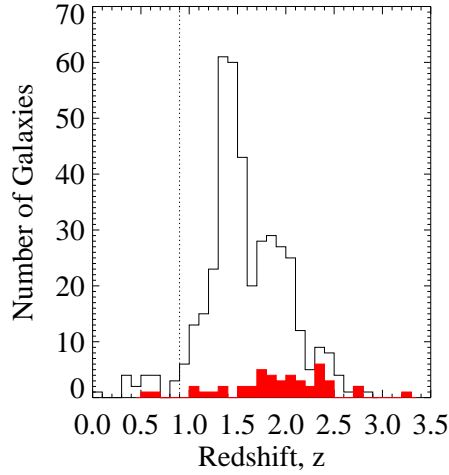


FIG. 2.— Histograms of photometric and spectroscopic redshifts for *sBzK* galaxies in ECDF-S. Upper curve indicates photometric redshifts. Lower filled (red), histogram indicates spectroscopic redshifts. Vertical dotted line indicates $z < 0.9$ galaxies that are excluded from analysis.

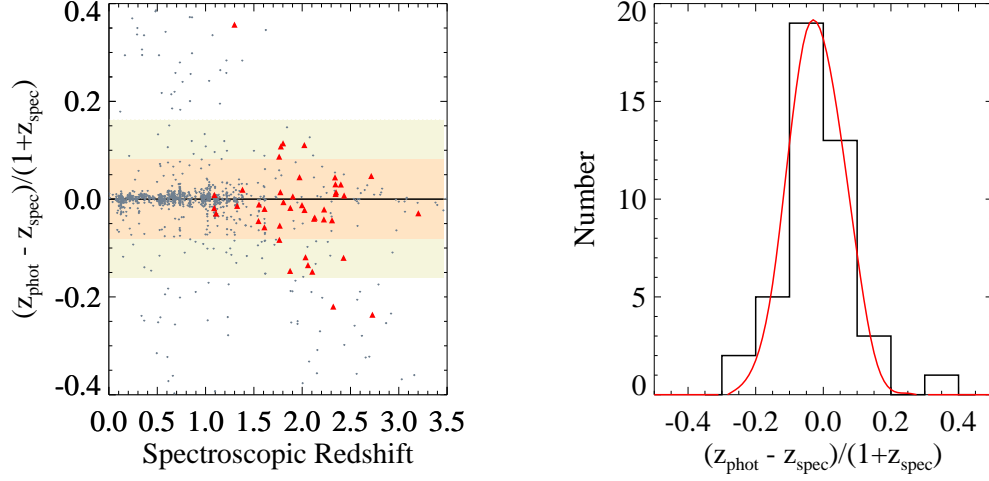


FIG. 3.— Left figure illustrates photometric redshift error, defined as $(z_{\text{phot}} - z_{\text{spec}})/(1 + z_{\text{spec}})$, vs. spectroscopic redshift for K selected galaxies in ECDF-S. Triangles (red) illustrate sBzK galaxies. 1σ and 2σ regions, determined from the histogram (right figure) are indicated by shading. Points (gray) illustrate all 1285 K selected galaxies for which spectroscopic and photometric redshifts are available. Right figure illustrates histogram of photometric redshift errors for sBzK galaxies along with a Gaussian fit (mean = -0.02 and $\sigma = 0.08$).

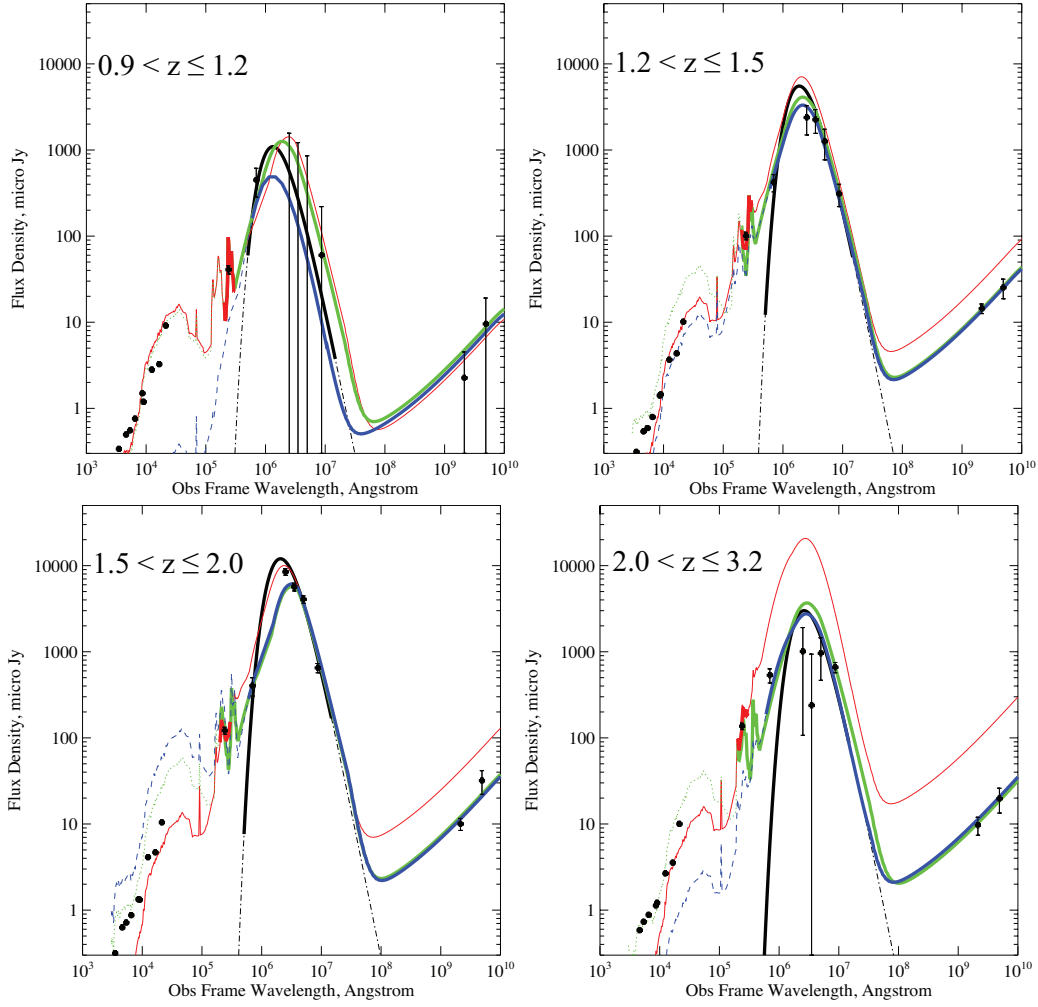


FIG. 4.— Spectral energy distributions of redshift binned sBzK galaxies obtained from stacking analysis, and fits to various models. Spectral flux density, in units of μJy , is plotted vs. observed frame wavelength, in units of Angstroms. UV through radio flux measurements are indicated by points with error bars. Curves indicate best fit models: dotted (green) CE01 template fitted to the $\lambda \geq 24\mu\text{m}$ spectrum, dashed (blue) CE01 template fitted to the $\lambda > 24\mu\text{m}$ spectrum, dot-dashed (gray) graybody (emissivity index, $\beta=1.5$) fitted to the FIR-submm peak, dot-dot-dash (red) CE01 template fitted to only the $24\mu\text{m}$ data point. For each model fit, the region of the spectrum used for the fit is indicated by the solid portion of the curve. Upper left: galaxies in the redshift range $0.9 < z \leq 1.2$; upper right $1.2 < z \leq 1.5$; lower left $1.5 < z \leq 2.0$; lower right $2.0 < z \leq 3.2$. See also Table 3 for fit details.

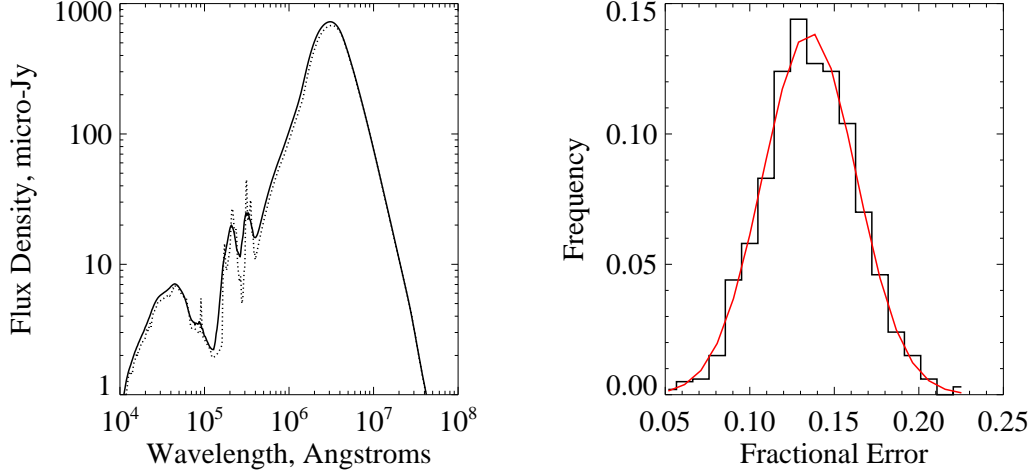


FIG. 5.— Left panel illustrates simulated, observed frame spectra for sBzK galaxies in the range $1.5 < z \leq 2.0$. The dotted curve indicates the best fit CE01 template placed at the median redshift, $z = 1.756$. The solid curve indicates the result of averaging 233 identical CE01 template sources, distributed in redshift according to the observed distribution of sBzKs, with photometric redshift errors added according to the distribution shown in Figure 3. Right panel illustrates the frequency distribution of L_{IR} fractional errors due to photometric redshift errors, for sBzK galaxies in the range $1.5 < z \leq 2.0$. Frequency is determined from the histogram of fractional errors and simulation with 1000 trials. Solid curve (red) indicates a Gaussian fit with mean = 0.14 and $\sigma = 0.03$. Thus photometric redshift errors caused L_{IR} for this redshift bin to be overestimated by 14% and contributed a scatter of 3%.

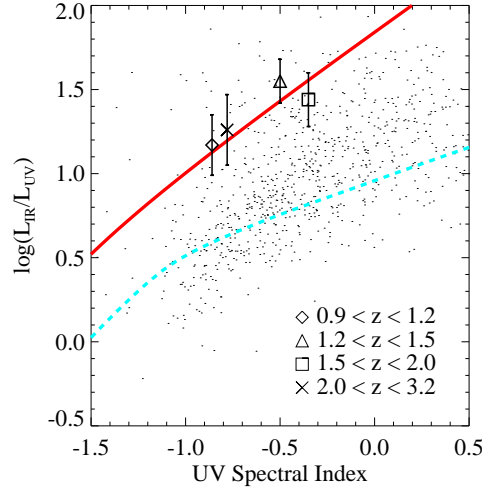


FIG. 6.— $\log(L_{IR}/L_{UV})$ vs UV spectral index, β (where $f_\lambda \propto \lambda^\beta$), for redshift binned sBzK galaxies and IR selected galaxies in the local universe. Symbols with error bars indicate redshift binned sBzK estimates. Points indicate star-forming and starburst galaxies in the local universe ($z < 0.3$) taken from Buat et al. (2010). The solid curve (red) indicates the relation for starburst galaxies from Meurer et al. (1999). The dashed curve (cyan) indicates a corresponding relation for normal star-forming galaxies in the local universe (Boissier et al. 2007).

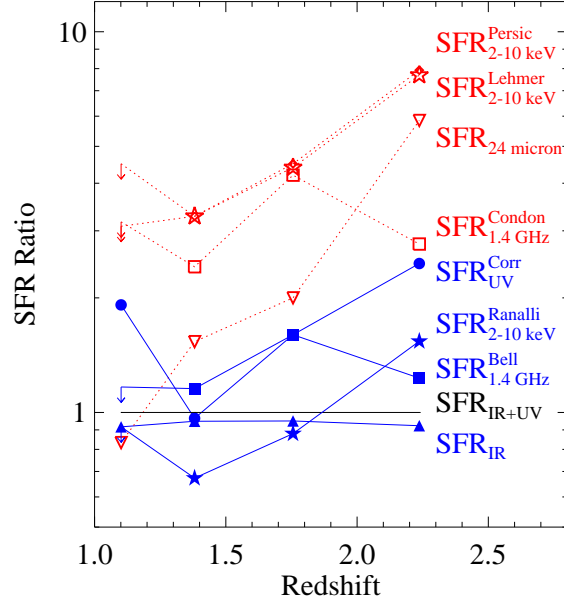


FIG. 7.— Ratio of SFR computed with various calibrations to the bolometric SFR estimate, SFR_{IR+UV} . Filled symbols (blue) indicate calibrations that are consistent with SFR_{IR+UV} to within errors in all redshift bins. Unfilled symbols (red) are inconsistent with SFR_{IR+UV} in at least one redshift bin. Upper limits are indicated by arrows. Lines connecting points are a guide to the eye.

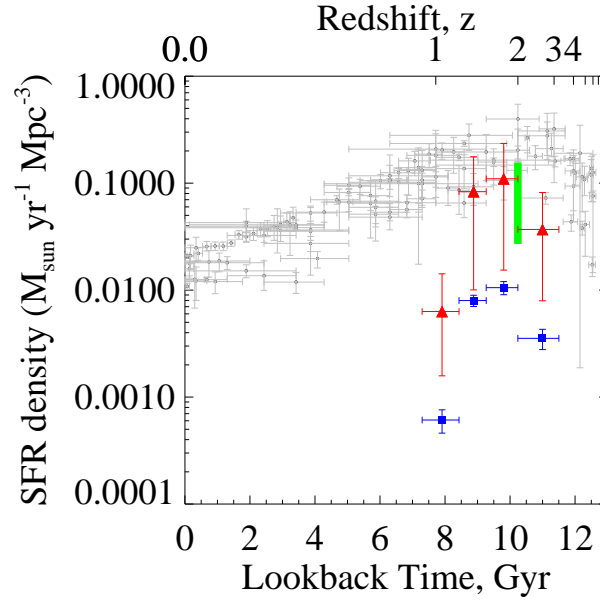


FIG. 8.— sBzK contribution to cosmic star formation history: Star Formation Rate Density (SFRD) vs. lookback time. Blue squares indicate SFRD contributed from redshift binned sBzK galaxies in MUSYC/ECDF-S. Red triangles indicate extrapolation to $K_{s,AB} < 23$ imaging depth, as discussed in the text. The green vertical bar indicates the range of the sBzK SFRD at $z \sim 2$ reported in Yoshikawa et al. (2010). Gray points are from the compilation of Hopkins (2007).

TABLE 1
 REDSHIFT BINNED SAMPLE OF STAR FORMING GALAXIES (sBzKs) IN THE
 ECDF-S

Redshift Range (1)	Median Redshift (2)	Number (z_{phot}, z_{spec}) (3)	Surf. Density, arc min ⁻² (4)	Vol. Density, Mpc ⁻³ (5)
$0.9 < z \leq 1.2$	1.101	49 (46,3)	0.05	6.56×10^{-5}
$1.2 < z \leq 1.5$	1.381	161 (157,4)	0.18	1.79×10^{-4}
$1.5 < z \leq 2.0$	1.756	233 (216,17)	0.26	1.37×10^{-4}
$2.0 < z \leq 3.2$	2.237	154 (132,22)	0.17	3.54×10^{-5}

NOTE. — Redshift binning scheme selected for this analysis. Column (1) indicate the redshift range for each bin. Column (2) indicates the median redshift of the sampled galaxies in each bin, and Column (3) shows the total number of galaxies in each bin, consisting of numbers of galaxies with photometric and spectroscopic redshifts, respectively, in parentheses. Column (4) indicates the density of galaxies on the sky in arc min⁻². Column (5) indicates the corresponding comoving volume density in Mpc⁻³.

TABLE 2
UV-RADIO AVERAGE FLUX DENSITIES FOR REDSHIFT BINNED sBzKs

Band (1)	λ (2)	$0.9 < z \leq 1.2$		$1.2 < z \leq 1.5$		$1.5 < z \leq 2.0$		$2.0 < z \leq 3.2$	
		S_ν (3)	σ_S (4)	S_ν (5)	σ_S (6)	S_ν (7)	σ_S (8)	S_ν (9)	σ_S (10)
U	0.35	0.34	0.02	0.31	0.02	0.32	0.02	0.23	0.01
B	0.46	0.49	0.02	0.54	0.03	0.63	0.03	0.58	0.03
V	0.54	0.55	0.03	0.59	0.03	0.72	0.04	0.73	0.04
R	0.65	0.76	0.04	0.79	0.04	0.87	0.04	0.88	0.04
I	0.86	1.50	0.08	1.40	0.07	1.33	0.07	1.13	0.06
z'	0.90	1.19	0.06	1.45	0.07	1.32	0.07	1.22	0.06
J	1.25	2.81	0.15	3.67	0.19	4.11	0.21	2.67	0.14
H	1.65	3.26	0.17	4.34	0.22	4.68	0.24	3.55	0.18
K	2.13	9.13	0.47	10.12	0.51	10.41	0.52	10.03	0.51
24 μm	24.00	40.80	4.50	100.70	10.20	121.60	11.40	136.50	11.90
70 μm	70.00	448.00	165.00	422.00	96.00	403.00	97.00	534.00	100.00
250 μm	250.00	-2684.36	1566.27	2383.17	887.57	8475.42	741.75	1008.16	901.19
350 μm	350.00	-2050.05	1217.80	2250.45	690.33	5661.50	577.76	238.18	701.00
500 μm	500.00	-2711.33	856.83	1254.78	486.30	4057.39	406.51	959.24	493.43
870 μm	870.00	60.00	160.00	310.00	90.00	650.00	80.00	660.00	90.00
1.4 GHz	2.1×10^5	<2.26	0.75	14.44	1.83	10.02	1.60	9.68	2.28
610 MHz	4.9×10^5	<9.55	3.18	25.19	6.45	31.88	9.79	19.70	6.31

NOTE. — UV-Radio Average flux densities for redshift binned sBzKs. Column (1) – Waveband. Column (2) – Effective, observed frame wavelength in units of μm . Columns (3,5,7,9) – Average, observed flux density in units of μJy for each redshift bin. 1.4 GHz and 610 MHz data in Column (3) indicate 3σ upper limits. Column (4,6,8,10) – Error in flux density in units of μJy for each redshift bin.

TABLE 3
REDSHIFT BINNED SBZK IR-RADIO FIT SUMMARY

Redshift (1)	Fit Type (2)	L_{IR} (3)	χ^2 (df) (4)	SFR_{IR} (5)
$0.9 < z \leq 1.2$	CE01 ($\geq 24 \mu\text{m}$)	0.6 ± 0.2	23.47(7)	11 ± 3
	CE01 ($> 24 \mu\text{m}$)	0.3 ± 0.3	18.96(6)	5 ± 5
	CE01 ($24 \mu\text{m}$)	0.6 ± 0.2	0.17(0)	10 ± 3
	GB (T=50 K)	0.5 ± 0.6	17.74(4)	9 ± 10
$1.2 < z \leq 1.5$	CE01 ($\geq 24 \mu\text{m}$)	3.2 ± 0.4	14.04(7)	55 ± 7
	CE01 ($> 24 \mu\text{m}$)	2.6 ± 0.2	4.64(6)	44 ± 4
	CE01 ($24 \mu\text{m}$)	5.2 ± 0.5	0.01(0)	89 ± 9
	GB	3.3 ± 0.5	3.49(4)	57 ± 8
$1.5 < z \leq 2.0$	CE01 ($\geq 24 \mu\text{m}$)	5.5 ± 0.8	48.40(7)	95 ± 14
	CE01 ($> 24 \mu\text{m}$)	6.1 ± 1.0	43.30(6)	106 ± 18
	CE01 ($24 \mu\text{m}$)	11.3 ± 3.0	0.01(0)	195 ± 51
	GB	11.8 ± 1.8	25.14(4)	203 ± 30
$2.0 < z \leq 3.2$	CE01 ($\geq 24 \mu\text{m}$)	6.9 ± 1.6	44.82(7)	120 ± 28
	CE01 ($> 24 \mu\text{m}$)	5.8 ± 1.5	22.15(6)	100 ± 26
	CE01 ($24 \mu\text{m}$)	44.2 ± 5.0	0.01(0)	761 ± 85
	GB (T=40 K)	4.2 ± 2.5	44.98(4)	72 ± 44

NOTE. — Column (1) indicates redshift range for the sample. Column (2) specifies the type of model fit (see text). Column (3) indicates the computed L_{IR} from the best fit model, in units of $10^{11} L_{\odot}$. Column (4) indicates the χ^2 value for the best fit, with degrees of freedom in parentheses. Column (5) indicates the SFR, in units of $M_{\odot} \text{ yr}^{-1}$, computed from the fit-derived IR luminosity. Errors correspond to 68% confidence intervals.

TABLE 4
REDSHIFT BINNED sBzK UV LUMINOSITY AND SFR ESTIMATES

Redshift (1)	Average of Individual Spectra							Avg. Spectrum
	L_{UV}^{Uncorr} (2)	β_{fit} (3)	$\log(\text{IRX})$ (4)	A_{1600} (5)	L_{UV}^{Corr} (6)	SFR_{UV}^{Uncorr} (7)	SFR_{UV}^{Corr} (8)	SFR_{UV}^{Corr} (9)
$0.9 < z \leq 1.2$	1 ± 0.3	-0.63	1.68	3.18	17 ± 5.6	1.3 ± 0.4	23 ± 8 (15)	13 ± 3
$1.2 < z \leq 1.5$	2 ± 0.6	-0.49	1.85	3.45	40 ± 16	2.0 ± 1.0	56 ± 22 (61)	48 ± 13
$1.5 < z \leq 2.0$	5 ± 5.4	-0.33	1.98	3.77	111 ± 57	7.0 ± 8.0	160 ± 79 (110)	140 ± 45
$2.0 < z \leq 3.2$	9 ± 5.2	-0.66	1.95	3.12	230 ± 200	12 ± 7.0	320 ± 280 (150)	150 ± 64

NOTE. — Column (1) indicates sample redshift range. Columns (2-8) correspond to unweighted averages of results from fitting individual galaxies in each redshift bin. Column (2) indicates uncorrected UV luminosity in units of 10^{28} erg s $^{-1}$ Hz $^{-1}$. Column (3) indicates the best fit slope, β , to the f_{λ} spectrum where $f_{\lambda} \propto \lambda^{\beta}$. Column (4) indicates the IR-UV ratio, $\log(S_{IR}/S_{1600})$. Column (5) indicates the attenuation in magnitudes at 1600 Å derived from the best fit spectral index, β . Column (6) indicates the dust corrected UV luminosity in units of 10^{28} erg s $^{-1}$ Hz $^{-1}$. Column (7) and (8) refer to SFRs derived from the UV luminosities in Columns (2) and (6) respectively, in units of M_{\odot} yr $^{-1}$. In Column (8) the median value is indicated in parentheses. Column (9) indicates the SFR from IRX- β correction applied to the unweighted average spectrum of galaxies in each redshift bin.

TABLE 5
REDSHIFT BINNED SBZK RADIO LUMINOSITY AND SFR ESTIMATES

Redshift Range (1)	$S_{1.4 \text{ GHz}}$ μJy (2)	$S_{610 \text{ MHz}}$ μJy (3)	α $S_\nu \propto \nu^\alpha$ (4)	$L_{1.4} \times 10^{22}$ W Hz^{-1} (5)	$\text{SFR}_{1.4 \text{ GHz}}^{\text{Condon}}$ $M_\odot \text{ yr}^{-1}$ (6)	$\text{SFR}_{1.4 \text{ GHz}}^{\text{Bell}}$ $M_\odot \text{ yr}^{-1}$ (7)
$0.9 < z \leq 1.2$	$< 2.26 (3\sigma)$	$< 9.55 (3\sigma)$	-1.70 ± 1.67	< 2.45	< 38	< 14
$1.2 < z \leq 1.5$	14.4 ± 1.8	25.2 ± 6.5	-0.66 ± 0.34	12.1 ± 1.7	140 ± 32	67 ± 120
$1.5 < z \leq 2.0$	10.0 ± 1.6	31.9 ± 9.8	-1.37 ± 0.41	29.6 ± 5.0	420 ± 250	160 ± 300
$2.0 < z \leq 3.3$	9.7 ± 2.3	19.7 ± 6.3	-0.84 ± 0.47	29.6 ± 7.1	360 ± 190	160 ± 300

NOTE. — Column (1) indicates the sample bin redshift range. Columns (2) and (3) indicate the median stacked flux at 1.4 GHz and 610 MHz respectively. 3σ upper limits are shown in the lowest redshift bin. Column (4) indicates the spectral index computed from these data. Column (5) indicates the derived rest frame 1.4 GHz luminosity. Column (6) indicates the computed SFR(0.1-100 M_\odot) according to Condon (1992). Column (7) indicates the computed SFR(0.1-100 M_\odot) according to Bell (2003). Upper limits are found for the $0.9 < z \leq 1.2$ flux measurements; these values are propagated to an upper limit SFR.

TABLE 6
REDSHIFT BINNED SBZK X-RAY FLUX, LUMINOSITY AND SFR ESTIMATES

Redshift Range (1)	Flux 0.5-2 keV (2)	Flux 2-8 keV (3)	Luminosity Rest 2-10 keV (4)	$\text{SFR}_{2-10 \text{ keV}}^{\text{Ranalli}}$ $M_\odot \text{ yr}^{-1}$ (5)	$\text{SFR}_{2-10 \text{ keV}}^{\text{Persic}}$ $M_\odot \text{ yr}^{-1}$ (6)	$\text{SFR}_{2-10 \text{ keV}}^{\text{Lehmer}}$ $M_\odot \text{ yr}^{-1}$ (7)
$0.9 < z \leq 1.2$	$< 4(1\sigma)$	$< 33(1\sigma)$	$< 6(1\sigma)$	$< 17(1\sigma)$	$< 54(1\sigma)$	$< 37(1\sigma)$
$1.2 < z \leq 1.5$	8.3 ± 3	34.0 ± 23	19 ± 6	39 ± 49	190 ± 72	190 ± 78
$1.5 < z \leq 2.0$	11.0 ± 2	44.0 ± 15	44 ± 7	88 ± 110	440 ± 110	450 ± 170
$2.0 < z \leq 3.2$	19.0 ± 2	96.0 ± 21	100 ± 13	200 ± 250	1000 ± 240	1030 ± 380

NOTE. — Column (1) — the sample bin redshift range. Column (2) — observed flux density in Chandra soft band (0.5-2 keV), in units of $10^{-18} \text{ erg s}^{-1} \text{ cm}^{-2}$. Column (3) — observed flux density in Chandra hard band (2-8 keV), in units of $10^{-18} \text{ erg s}^{-1} \text{ cm}^{-2}$. Column (4) — the luminosity in rest frame (2-10 keV), computed from observed, soft band flux, assuming spectrum with photon index, $\Gamma=1.2$ and $E_c=20 \text{ keV}$, at the median redshift. Units are $10^{40} \text{ erg s}^{-1}$. Column (5) — SFR from the method of Ranalli et al. (2003). Column (6) — SFR from the method of Persic et al. (2004). Column (7) — SFR from the method of Lehmer et al. (2010). All SFRs in units of $M_\odot \text{ yr}^{-1}$ assuming Salpeter IMF (0.1 - 100 M_\odot).

TABLE 7
REDSHIFT BINNED sBzK STAR FORMATION RATE SUMMARY

Redshift (1)	SFR _{IR} (2)	SFR _{24μm} (3)	SFR _{UV} ^{Corr} (4)	SFR _{1.4GHz} ^{Condon} (5)	SFR _{1.4GHz} ^{Bell} (6)	SFR _{2–10keV} ^{Ranalli} (7)	SFR _{2–10keV} ^{Persic} (8)	SFR _{2–10keV} ^{Lehmer} (9)	SFR _{IR+UV} (10)
0.9 < z ≤ 1.2	11±2.8	9.9±2.6	23±8	<38	<14	<17	<54	<37	12±2.8
1.2 < z ≤ 1.5	55±7.0	89±8.5	56±22	140±32	67±120	39±49	190±72	190±78	58±7.0
1.5 < z ≤ 2.0	95±14	190±51	160±79	420±250	160±300	88±110	440±110	450±170	100±14
2.0 < z ≤ 3.2	120±28	760±85	320±280	360±190	160±300	200±250	1000±240	1030±380	130±28

NOTE. — Star formation rates for redshift binned sBzKs. Column (2) – SFR from integrated IR luminosity using CE01 template fits to MIR-radio photometry ($\lambda \geq 24\mu\text{m}$). Column (3) – SFR from CE01 template fit to 24 μm data only. Column (4) – SFR from average of individual fits to UV continuum with dust correction. Columns (5) and (6) – SFR from median, stacked 1.4 GHz flux using the method of Condon (1992) and Bell (2003) respectively (1st row – a 3σ upper limit). Columns (7-9) – SFR from soft band X-ray data using the method of Ranalli et al. (2003), Persic et al. (2004) and Lehmer et al. (2010) respectively. Column (10) – the total SFR from the sum of Column (2) and corresponding uncorrected UV SFRs taken from Table 4. Units are $\text{M}_{\odot} \text{ yr}^{-1}$ for all columns.